COSMOGENIC ^{10}Be SURFACE EXPOSURE DATING AND NUMERICAL MODELING OF LATE PLEISTOCENE GLACIERS AND LAKES IN NORTHWESTERN NEVADA

A Thesis
Submitted to the Graduate Faculty
of the
North Dakota State University
of Agriculture and Applied Science

By

Kaitlyn Chelsea Fleming

In Partial Fulfillment of the Requirements
for the Degree of
MASTER OF SCIENCE

Major Program:
Environmental and Conservation Sciences

April 2019

Fargo, North Dakota

North Dakota State University
Graduate School

Title

Cosmogenic ^{10}Be Surface Exposure Dating and Numerical Modeling of Late Pleistocene Glaciers and Lakes in Northwestern Nevada

By

Kaitlyn Chelsea Fleming

The Supervisory Committee certifies that this ***disquisition*** complies with North Dakota State University's regulations and meets the accepted standards for the degree of

MASTER OF SCIENCE

SUPERVISORY COMMITTEE:

Benjamin Laabs
Chair

Stephanie Day

Xuefeng Chu

Approved:

4/11/19
Date

Craig Stockwell
Department Chair

ABSTRACT

This thesis focuses on the glacial record in the Pine Forest and Santa Rosa Ranges located in the northwestern Great Basin. Seventeen cosmogenic exposure ages in the two ranges are consistent with observations elsewhere in the Great Basin where glacier maxima and lake highstands in the northwestern Great Basin occurred at ~18-17 ka. Developing chronologies of moraines in the Santa Rosa and Pine Forest Ranges has helped to precisely limit the relative timing of glacier and lake maxima. Model results are consistent with previous studies of the LGM (21-20 ka) interval and early Heinrich Stadial 1 (18-17 ka) intervals, such that the northern Great Basin was colder with near-modern precipitation during the LGM and likely greater than modern precipitation during the subsequent interval 18-17 ka. Overall, the chronology of glacial deposits in the northwestern Great Basin and inferred climate during the last glaciation show consistency across the northern Great Basin.

ACKNOWLEDGEMENTS

Firstly, I would like to express my sincere gratitude to my advisor Dr. Ben Laabs for the continuous support of my Master's study and related research, for his patience, motivation, and immense knowledge. His guidance helped me out in the field, all the time of research, and writing this thesis. I could not have imagined having a better advisor and mentor for my Master's study. Besides my advisor, I would like to thank the rest of my committee: Dr. Day and Dr. Chu for their insightful comments and encouragement. I would also like to thank my fellow lab-mates for the stimulating discussions as well as all the great times we have had out in the field and in the lab. Also, I thank my friends and professors from my undergraduate institution, Sonoma State University. Last but not least, I would like to thank my family: my parents and to my uncles, aunts, grandparents, and cousins for supporting me throughout my college career and my life in general.

DEDICATION

My Mom

For someone, who has always been there for me and who taught me that hard work and dedication really does pay off. Love you more than a million Swedish fish.

My Dad

For encouraging and supporting me and for bogurt yogurt every Friday. Love you dad.

My Grandparents

A grandmother and grandfather, who taught me to dance. Another grandmother, who taught me how to make a mean banana bread and a grandfather/pop pop, who gave me my love for the outdoors.

TABLE OF CONTENTS

LIST OF FIGURES

LIST OF APPENDIX TABLES

LIST OF APPENDIX FIGURES

CHAPTER 1: INTRODUCTION

The Pleistocene Epoch of the Quaternary Period is defined as the time period that began 2.6 million years ago and lasted until approximately 11,700 years ago (Walker and others, 2018). The Pleistocene is best characterized by the occurrence of numerous glaciations. Glaciations are intervals of ice expansion across the continents in the geologic past. They are uncommon over the duration of Earth history, but are quite common over the Quaternary Period. The remains of these glaciations can be seen in the geologic record.

At the height of the last glaciation, termed the Last Glacial Maximum (LGM), vast ice sheets covered much of North America, northern Europe, and Asia. The ice sheets affected the Earth's climate profoundly by causing drought, desertification, and a large drop in global sea level. Throughout the world, climates during the LGM were cooler and almost everywhere drier. This has been studied using various methods, including numerical modeling of glaciers and lakes. The LGM can be defined as the period of maximum global ice volume near the end of the last glaciation of the Pleistocene Epoch. ^{14}C, ^{10}Be, and ^{3}He ages of glacial deposits representing the last glaciation span the interval from 10,000 to 50,000 years ago have been used in order to constrain the timing of the Last Glacial Maximum in terms of global ice sheet and mountain glacier extent (Clark et al. 2009). Between 33.0 and 26.5 ka, ice sheets grew to their maximum positions. This was in response to climate where there were decreases in northern summer insolation, tropical Pacific sea surface temperatures, and atmospheric CO_2 (Clark et al. 2009). A minima in these climate forcing's resulted in almost all of the ice sheets being at their LGM positions from approximately 26.5 to 19 to 20 ka (Clark et al. 2009). Additionally, due to an increase in northern summer insolation, which provided the source for a rise in sea level, the onset of the Northern Hemisphere deglaciation occurred between 19 to 20 ka (Clark et al. 2009).

The onset of deglaciation of the West Antarctic Ice Sheet, however, occurred between 14 and 15 ka, which is consistent with evidence that this was the source for a rise in sea level at approximately 14.5 ka (Clark et al. 2009).

During the Last Glacial Maximum (LGM), mountain glaciers occupied numerous mountains in the Great Basin of the southwestern United States and pluvial lakes (body of water that accumulated in a basin due to an increase in moisture availability resulting from temperature and precipitation changes) formed in intermountain valleys (Figure 1). Osborn and Bevis (2001) provide the most recent glacial geologic mapping and a useful overview of Great Basin glacial geology. They identified approximately forty individually named ranges, plateaus, and massifs draining wholly or partly into the Great Basin showing evidence of Pleistocene glaciation (Osborn and Bevis, 2001). The ranges of focus for this study include the Ruby Mountains/East Humboldt Range, Wasatch Range and Uinta Mountains, and the northwest Nevada Ranges, including the Pine Forest and Santa Rosa Ranges. A majority of the world's deserts expanded, exceptions to this, were in what is now the southwestern United States. A change in atmospheric circulation brought an increase in rainfall to areas that today, are represented by deserts. Due to the increase in rainfall, large pluvial lakes formed in topographically closed areas of the Great Basin region of the Southwest.

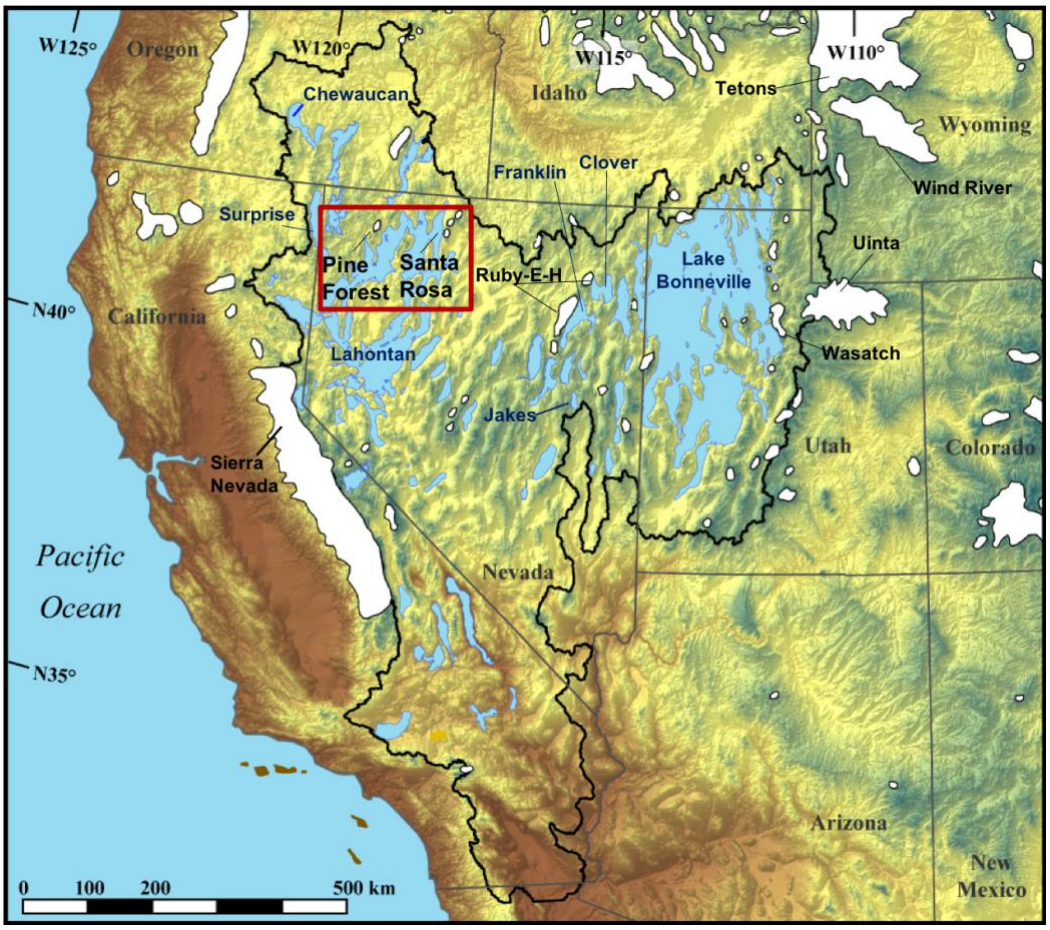

Figure 1. Shaded relief map of the Great Basin (black outline) and neighboring regions in the western United States, with extents of Great Basin lakes (blue) and mountain glacier systems (white). Lake extents are from Reheis (1999) and glacier systems are from Pierce (2003). Mountain glacier systems for this study area are outlined in red.

There are three groups of glacial deposits of the last glaciation that can be distinguished as a family of moraines termed the "Tioga", "Angel Lake", and "Pinedale." More specifically, "Tioga" is the term for the last glaciation in the Sierra Nevada, "Pinedale" for the last glaciation in the Rocky Mountains, and "Angel Lake" for the last glaciation in the Great Basin. They likely represent the same ice advances at similar times, but are found in different places and are difficult to correlate to one another, which is the main reason why methods of numerical dating of glacial deposits is needed to establish a chronology of the last glaciation. Across the Great Basin, moraines of the Angel Lake Glaciation are generally thick, hummocky, lobate piles of till

rather than looping ridges. Such moraines are likely a product of heavy glacial debris loads, as well as glacial advance, retreat, and re-advance to the same positions numerous times (Osborn and Bevis, 2001). Pre-Angel Lake deposits from early glaciations of the Quaternary Period occur in multiple Great Basin ranges, but it is difficult to determine if these deposits are equivalent in age to one another (Osborn and Bevis, 2001). The evidence that we see for glacial geology in the Great Basin, not only includes these different types of moraines, but also U-shaped valleys, abandoned cirque headwalls, and numerous other glacial erosional landforms. Knowing the glacial history of the Great Basin gives us a starting point for looking at the changes in climate throughout the Late Pleistocene that accompanied these glacial advances, retreats, and re-advances.

The already marginal supply of surface water in parts of the northern Great Basin is shrinking due to diminishing freshwater lakes, mountain snow, and groundwater (Griffin and Anchukaitis, 2014). The public demand for surface water remains, however especially in cities with rising populations such as Salt Lake City, Utah and Reno, Nevada. A clearer understanding of how mountain snow and surface water responded to warming during the deglacial period can guide surface water resource management practices in the 21st century as climate in the region is forecast to warm. Developing the glacial record through cosmogenic ^{10}Be surface exposure dating of moraines and numerical modeling of glaciers and lakes can help to reveal the temporal pattern of glaciation and accompanying changes in Pleistocene climate. Specifically, identifying the relative timing of glacier maxima and lake highstands, and then the changes in temperature and precipitation accompanying glacier and lake maxima can help to understand the drivers of climate change during the last glaciation and deglaciation.

In order to infer Late Pleistocene precipitation and temperature conditions in these once glaciated settings in the Great Basin, it is important to develop the glacial geologic record in space and time. The chronology of glacial deposits in the northwestern Great Basin is unknown, and developing it will bridge a data gap between dated glacial records in the northeastern Great Basin and the Sierra Nevada and Cascade Ranges to the west. Cosmogenic ^{10}Be surface exposure dating of moraine sequences has been done throughout the Great Basin and is an excellent tool for determining how long a rock has been exposed to Earth's surface. Previous field study in the northwestern Great Basin (B. Laabs and J. Munroe, written communication) identified well-preserved moraine sequences in the Santa Rosa and Pine Forest Ranges suitable for surface exposure dating. Although other mountains in the northwest Great Basin were also glaciated, moraines in those mountains did not feature quartz-rich materials that were suitable for cosmogenic ^{10}Be exposure dating. Cosmogenic exposure dating hasn't been done yet in many areas of the northwest Great Basin. This study focused on the Pine Forest and Santa Rosa Ranges of the northwest Great Basin in order to determine the timing of the last glaciation in the northwest Great Basin.

A large number of studies involving the study of mountain glacial geology or glacier chronology, or any other paleoclimate synthesis involving glaciation have used cosmogenic-nuclide exposure dating to date glacial deposits (Balco et. al 2011). This type of exposure dating has proven very useful for dating glacier advances and retreats. This is because temperate glaciers (with an ice temperature at the pressure melting point) are effective agents of erosion and therefore, can create fresh rock surfaces. Due to the fact that the bed of a glacier is also hidden from the cosmic-ray flux by the overlying ice, subglacial erosion acts to produce fresh rock surfaces whose cosmogenic-nuclide record is negligible (Balco et al. 2011). This is also true

of the products of subglacial erosion. The clasts that are detached from a glacier bed that is eroding and is transported by ice can also be expected to have a negligible cosmogenic-nuclide concentration. When these clasts have been transported to the ice margin and are then deposited as a moraine, they become exposed to the cosmic-ray flux and begin the accumulation of cosmogenic nuclides (Balco et al. 2011). As a result, cosmogenic surface exposure dating can be used to date the emplacement of moraines as well as ice retreat. However, it is important to note that there a number of factors that go into cosmogenic ^{10}Be surface exposure dating of moraines, such as having a good sampling strategy, making sure the measurements and observations needed to calculate an exposure age are accurate, and knowing the nuclide production rate. All of these factors, including the methodology behind surface exposure dating as well as how to calculate a surface exposure age are discussed in Chapter 3.

Dating glacial landforms helps us to understand past ice sheet extent and rates of ice sheet extension. By dating these landforms, we are then able to model the ice extents depending on where samples were collected for the recessional and terminal moraines. Glacial geologists have been using paleoglaciers for many years to understand past climate. Researchers have relied on reconstructions of paleoglacier equilibrium line altitudes (ELAs) as a way to infer past temperature and precipitation changes. The standard methods of interpreting the paleoclimates recorded in glacial geomorphic features rely on estimates of paleoglacier shape and generally assume that relationships between mass balance gradient and ELA of modern glaciers apply equally to glaciers of differing climates (Plummer and Phillips, 2003).

Paleoclimates that are related to paleoglacial features are inferred from the depression of ELA relative to that of modern glaciers. The process that uses ELA to infer paleoclimate typically involves estimates of a series of glacial parameters both for the paleoglacier and for the

modern glacier. First, geomorphic evidence, such as a small terminal moraine is used to estimate the surface of the paleoglacier. Next, the ELA of the reconstructed glacier is estimated by applying an empirical relationship between glacier surface area that is obtained from modern glaciers and ELA position (Plummer and Phillips, 2003). The most common method that is applied, determines the paleo-ELA by inferring an accumulation area to total glacier area ratio of approximately 0.65 (a value derived from the study of modern glaciers) (Plummer and Phillips, 2003). Lastly, by comparing the paleo-glacier ELA with ELAs of modern glaciers from the same area, the ELA depression is estimated. However, in multiple cases, glaciers may have entirely vanished from the region of interest, in which case the modern ELA also has to be estimated. Every step in this process involves some uncertainty, including difficulties that stem from the fact the climate sensitivity of the larger glaciers of the past may have been significantly different than that of their modern counterparts (Plummer and Phillips, 2003). The estimation of ELAs assumes a 1-D relationship between mass balance and elevation. Plummer and Phillips, however, developed a 2-D modeling approach, which has proven to be a more preferable method of using reconstructed mountain glaciers to infer climate of the past. A modeling approach provides a means of building 'from scratch,' the glaciers that would develop under various climate conditions (Plummer and Phillips, 2003).

Even though there have been many inferences of how climate changed in the northern Great Basin area during and after the last glaciation, estimates of temperature and precipitation during times of glacier and lake maxima in the Great Basin are variable. For example, recent hydrologic modeling studies of the Lake Surprise and Jakes Lake conclude that lake highstands in these valleys during the latter part of the last glaciation were accompanied by temperature depressions of 5-7° C from modern and precipitation 75-90% greater than modern (Ibarra et al.,

2014; Barth et al., 2016), whereas other studies of glacial and lake records have concluded colder and drier climate accompanying lake highstands (e.g., Lyle et al., 2012). Speleothem stable isotopes are useful, continuous records of changes in effective moisture during the last glaciation (e.g., Lachniet et al., 2014; Oster and Kelly, 2016), but they do not by themselves distinguish changes in temperature and precipitation. A correlation between Great Basin- $\delta^{18}O$ values and the level of Lake Lahontan shows that lake highstands were associated with low speleothem $\delta^{18}O$ values between 20 and 14 ka, and low lake levels with high $\delta^{18}O$ values (Lachniet et al. 2014). Cold periods were supplied by high latitude moisture delivered from a northerly source region in order to get maximum lake levels (Lachniet et al. 2014). Lake levels that were low coincided with both dry and warm climate conditions during the earlier part of the Holocene, but then shifted towards cooler and wetter conditions in the later part of the Holocene (Lachniet et al. 2014). These inferred climate conditions are associated with the Fallon Lake cycles in the Lahontan Basin. Lachniet's et al. (2014) new 175,00 year $\delta^{18}O$-Great Basin record suggests similar pluvial lake expansions may have happened during other periods of cool temperatures as documented for MIS-2 at Pyramid Lake, for MIS-3 cool events in Lake Bonneville, during the penultimate glacial maximum (MIS 6), and potentially during MIS 5d when $\delta^{18}O$ values reach minimum values, which are consistent with correlations of deep lake cycles with glacial maxima (Lachniet et al. 2014).

Available glacial chronologies and well-dated lake highstands and regressive phases determined by radiocarbon ages of shoreline deposits reveal a series of time intervals during the last Pleistocene glaciation when the extents of mountain glaciers and neighboring paleolakes are both known. The first interval coincides with the latter part of the Last Glacial Maximum (LGM) at an interval of 20-21 ka. Previous studies suggest that glaciers were at their maximum extents,

but most Great Basin lakes were below the level of their highstand shorelines. A recent study conducted by Oster et al. (2015) examined geologic records of precipitation and output of general circulation models representing the latter part of the Last Glacial Maximum. Oster et al. (2015) compared a network of precipitation-sensitive proxy records from western North America along with a group of LGM (21 ka) general circulation model simulations that were carried out as part of phases two and three of the Paleoclimate Modeling Intercomparison Project (PMIP2 and PMIP3) in order to determine which model outputs best match proxy records of western North America precipitation and the mechanisms that produced these patterns (Oster et al. 2015). The proxies included records from glaciers, speleothems, lakes, packrat middens, and groundwater deposits. For each record, hydroclimatic response time during the LGM was classified as indicative of wetter, drier, or no change relative to pre-industrial conditions (Oster et al. 2015). Similar to modern precipitation responses to interannual and decadal variability, the LGM proxies suggest a precipitation dipole (Oster et al. 2015). A precipitation dipole consists of two areas with contrasting precipitation patterns. The precipitation dipole suggests wetter than modern conditions in the southwestern United States, drier conditions in the Pacific Northwest through the Rockies, as well as a northwest-southeast transition zone from wetter to drier conditions across the northern Great Basin during the LGM (Oster et al. 2015).

The second time interval of known glacier and lake extent coincides with the earlier part of the last deglaciation (succeeding the LGM) at an interval of 18-16 ka. The interval 18-16 ka, featured the expansion of Lake Bonneville, Lake Lahontan, Lake Franklin, Lake Clover, Jakes Lake, and others across the northern Great Basin. This suggests that climate shifted to favor the expansion of lakes. Glaciers in the Wasatch Mountains, Ruby Mountains, and East Humboldt Mountains were at or near their maximum extent during this time, as were some glaciers in the

Uinta Mountains (Quirk et al. 2016). This suggests a climate favorable for both glaciers and lakes, possibly wetter than the preceding interval of the late LGM (Benson et al. 2011). In the northwest Great Basin, however, Lake Surprise reached its maximum extent while glaciers in the Santa Rosa and Pine Forest Ranges were most likely retreating.

The interval of 17-15 ka overlaps with Heinrich Stadial 1 (ca. 17.5-14.7 ka; Hemming, 2004). Heinrich events are caused by the discharge of icebergs into the North Atlantic, which disrupts the flow of heat in the ocean towards higher latitudes and can result in cooling of the northern hemisphere. This, in turn, disrupts atmospheric circulation and results in changing winds as described by Hemming (2004). When compared to glacial conditions, there seems to be a pattern for wetter conditions along the western North Atlantic margin during Heinrich events, but more extreme cold/dry glacial conditions during Heinrich intervals on the eastern North Atlantic margin (Hemming, 2004). This difference in Heinrich events compared to glacial conditions, as well as the geographic distribution of sites can provide clues to the driving forces of climate change (Hemming, 2004). The Heinrich Stadial 1, which spanned 17.5-14.7 ka suggests that there was the delivery of more moisture from the Pacific Ocean to parts in the northwestern Great Basin, suggesting wetter and colder conditions. The interval 17-15 ka featured pluvial lakes, including Jakes Lake, Lake Franklin, Lake Clover, Lake Bonneville, and others in the northern Great Basin to obtain maximum levels (Quirk et al., 2016).

The northwestern Great Basin features a glacial record that is undeveloped relative to other sectors of the region and can help to determine how climate changed during the end of the last glaciation and the subsequent deglaciation. The research described here focuses on (1) the relative timing of glacier maxima in the northwest Great Basin and (2) setting precise limits on temperature and precipitation based on combined results of numerical mountain glacier modeling

and lake modeling. In order to develop the glacial record, cosmogenic ^{10}Be exposure dating of moraines and numerical modeling of paleoglaciers were applied to valleys in two separate mountains. Additionally, this thesis also combines glacier and lake modeling results from the northcentral Great Basin to identify a unique set of temperature and precipitation combinations for a brief interval during the last glaciation.

CHAPTER 2: REGIONAL SETTING

Great Basin

During the LGM, glaciers occupied numerous mountains in the Great Basin, including the Wasatch, Uinta, Sierra Nevada, and the Pine Forest and Santa Rosa Ranges (Osborn and Bevis, 2001), (Figure 1) and pluvial lakes formed in the intermountain valleys (Reheis, 1999, 2014). Together, these glaciers and lakes recorded significant changes in regional climate during the last glaciation (26.5-19.0 ka; Clark et al., 2009) and deglaciation (19.0-11.5 ka). These records provide one of the best-preserved regional climatic records in the world and constitute an ideal dataset for numerical models (glacial and lake) seeking to reconstruct past climate.

The Great Basin spans nearly all of Nevada, much of Oregon and Utah, and portions of California, Idaho, and Wyoming (Figure 1). It is well-known for both its arid climate and the basin-and-range topography. The Great Basin is a region of internal drainage that has experienced crustal thinning and deformation accommodated by extensive faulting. There are approximately forty ranges, plateaus, and massifs draining wholly or partly into the Great Basin and show definitive evidence of Late Pleistocene glaciation (Osborn and Bevis, 2001). The Great Basin is bounded on the west by the Sierra Nevada and Cascade Ranges, on the south by part of the Mojave Desert drained by the Colorado River, on the south and east by the Colorado Plateau, and on the north by the Snake River Plain (Osborn and Bevis, 2001). The Great Basin contains broad valleys with interspersed elongate, north-south trending, fault-bounded mountain ranges. The highest peak in the Nevada area of the Great Basin is Wheeler Peak, rising at an elevation of 4,010 m. The Great Basin has a characteristic temperature regime of hot summers and cold winters and the region is usually dry, with most areas receiving less than 20 cm of rainfall per year.

The Great Basin includes valleys, basins, lakes and mountain ranges of the Basin and Range Province (Figure 2). The precipitation in the region evaporates, sinks underground, or flows into lakes. Most of the Great Basin's precipitation comes from snow, and the precipitation that neither evaporates nor is extracted for human use will sink into the groundwater aquifers. The term "Great Basin" is somewhat misleading as the region is actually made up on many small basins. The Great Salt Lake, Pyramid Lake, and the Humboldt Sink areas are but a few of which drains the Great Basin. In the northwestern part of the basin, large Pleistocene lakes formed, which include, but are not limited to, Lakes Bonneville, Lahontan, Franklin, Clover, and others. Most of these Pleistocene lakes were quite large in size and include highstands that represent key intervals of the last pluvial cycle.

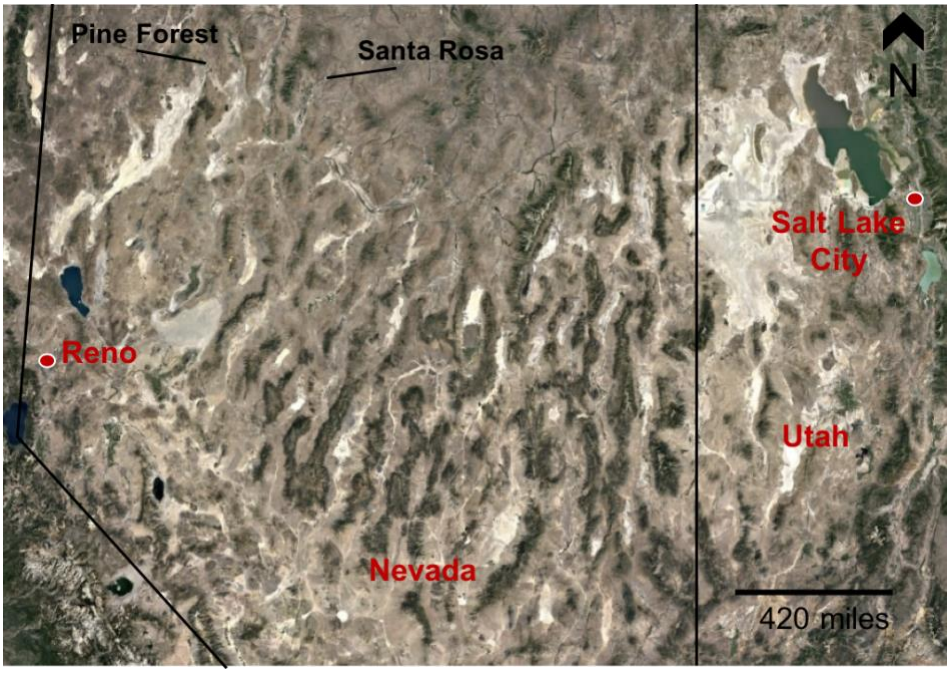

Figure 2. Image taken from Google Earth showing where the Pine Forest and Santa Rosa Ranges are relative to two major cities (Reno and Salt Lake City)

Santa Rosa Range

The Santa Rosa Range is a mountain range located in Humboldt County, Nevada, United States. Most of the range is included within the Humboldt-Toiyabe National Forest. The highest

peaks in the range are Granite Peak (2,966 m) and Santa Rosa Peak (2,956 m). The range also includes another peak termed Paradise peak, which is of modest elevation. These peak elevations are very important due to the fact they were surrounded by Pleistocene glaciers. The range extends for approximately 120 km north from Winnemucca Mountain near Winnemucca through eastern Humboldt County to the Oregon border (Figure 3). The mountains are composed of Mesozoic metasediments overlain by Tertiary rhyolitic and andesitic flows and tuff, and intruded by small granitic plutons (Stewart, 1980; Vikre, 1985). There are over six glaciated valleys, heading on the north flank of Granite Peak, the north and east flanks of Santa Rosa Peak, the north flank of Paradise Peak, and against unnamed headwalls 1.5 km south and 2.2 km SSW of Paradise Peak respectively (Osborn and Bevis, 2001). In these glaciated valleys are morainal lobes, extending down from cirque headwalls, characteristic of moraines deposited during the Angel Lake Glaciation. There are a few terminal moraines near Granite Peak that were used for cosmogenic ^{10}Be surface exposure dating and numerical modeling. The moraines near Paradise Peak and Santa Rosa Peak, however do not feature well-defined morainal shapes, and unfortunately cannot be used for reconstructing glacier shapes or surface exposure dating.

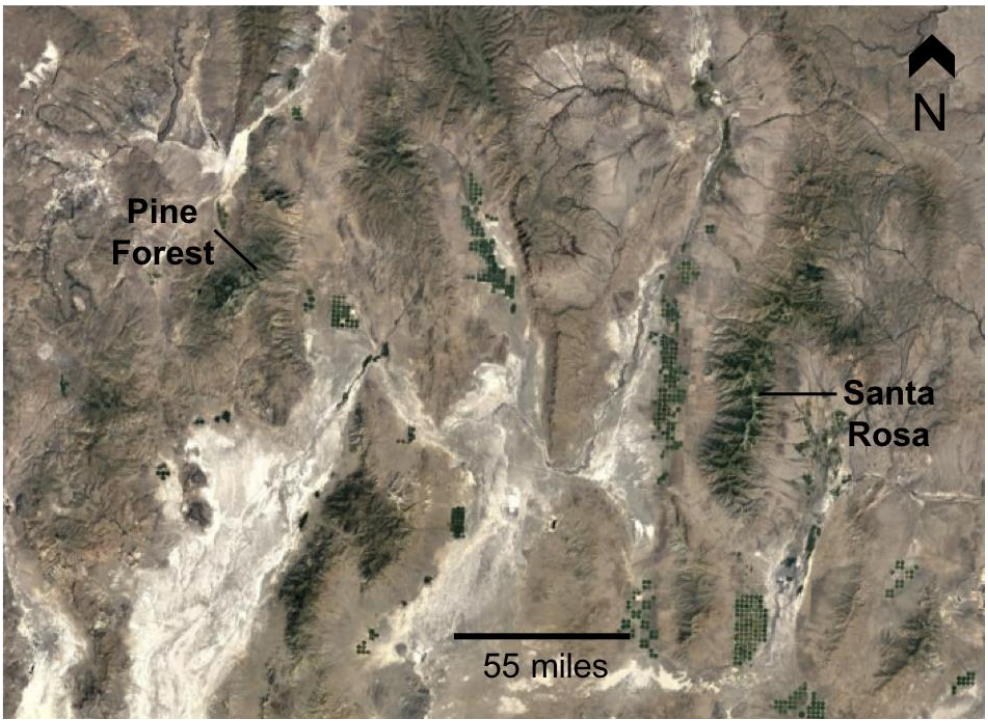

Figure 3. Image taken from Google Earth showing a zoomed in image of the Pine Forest and Santa Rosa Ranges

Pine Forest Range

The Pine Forest Range (also known as the Pine Forest Mountains) is located in Humboldt County, Nevada, United States and is just north of the Black Rock Desert. The Pine Forest Mountains are within the northwestern part of the Great Basin (northern part of the Basin and Range province), near Denio, Nevada (Figure 3). In the glaciated regions, the bedrock has been classified as granodiorite (Smith, 1973). The generalized geologic map that was created by Smith (1973), shows morainal deposits in the drainages of Blue Lake/Onion Valley Reservoir, Leonard Creek, Alder Creek, the fork of Big Creek just east of Blue Lake, and the fork of Big Creek that heads northwest of Blue Lake (Osborn and Bevis, 2001).

The Pine Forest Range is of modest elevation with only a few closely spaced, relatively high summits, the highest of which is Duffer Peak at an elevation of approximately 2,865 m (Osborn and Bevis, 2001). The valleys surrounding this peak include evidence for a minimum of

three glaciers. There is a large moraine loop impounding Blue Lake and has been determined to be a product of the Angel Lake Glaciation, and that indistinct moraines south and east of Onion Valley Reservoir are Lamoille in age. Small cirque moraines on the order of 100 m out from the head of the Blue Lake cirque and the head of the cirque 700 m southwest of Duffer Peak (Osborn and Bevis, 2001). The outermost terminal moraine in one of the glaciated valleys was targeted for cosmogenic ^{10}Be surface exposure dating and numerical modeling. Additionally, a recessional moraine further upvalley from the terminal moraine, close to Blue Lake, was also targeted for cosmogenic ^{10}Be surface exposure dating and numerical modeling.

Lake Franklin

Pluvial Lake Franklin was relatively small compared to Lakes Bonneville and Lahontan, but is situated near the well dated moraine sequences in the Ruby and East Humboldt Mountains (Figure 1). Lake Franklin covered approximately 1100 km^2 of the Ruby Valley of northeastern Nevada during the last glacial cycle (Munroe and Laabs, 2013). A shallower (<10 m) arm of the lake extended eastward into North Butte Valley (Munroe and Laabs, 2013). Today, the floor of the Ruby Valley is relatively flat and has a gradual slope. The unglaciated Medicine and Maverick Springs Ranges borders the valley to the east and the glaciated Ruby Mountains borders the valley to the west (Munroe and Laabs, 2013). Most of the streams and rivers in the Lake Franklin watershed are ephemeral (Munroe and Laabs, 2013). The largest fluvial system is the Franklin River, which historically, has carried water from the northern Ruby Valley to a playa that hosts Franklin Lake. Now, water is only present during spring snowmelt due to upstream diversions (Munroe and Laabs, 2013). The floor of the southern Ruby Valley presents a different scenario, however. Approximately 200 springs discharge groundwater to a 55 km^2 perennial wetland known today as the Ruby marshes (Thompson, 1992).

The late Pleistocene history of Lake Franklin has received little attention prior to a study conducted by Munroe and Laabs (2013). Shoreline features that were well-preserved and recorded the former presence of a lake in the Ruby Valley were recognized by geologists in the 19th century, but they were poorly considered evidence of a bigger regional lake (Simpson, 1876). However, later studies realized that these shorelines reflected a lake confined to the Ruby Valley (Russell, 1885), which was named Lake Franklin (Sharp, 1938). Munroe and Laabs (2013), constructed a hydrograph that is based on radiocarbon dating of gastropod shells. Results collected by Munroe and Laabs (2013), indicate that during the LGM at 24-21 ka, Lake Franklin covered approximately 43% of its maximum extent, where the level of the water averaged 1823m. During the LGM at 21-17 ka, Lake Franklin expanded to cover 60% of its highstand area, where the lake level was again stable at 1830 m (Munroe and Laabs, 2013). The pluvial maximum of Lake Franklin at 17-16 ka began with a rise to a highstand elevation of 1850 m, which was synchronous with highstands in a number of surrounding pluvial lakes (Munroe and Laabs, 2013). After this interval in time, there continued to be a series of transgression and regression periods. Lake Franklin is located midway between Lakes Lahontan and Bonneville, which offers the potential for comparison with other regional paleoclimate records.

Glacial Features

Moraines

Moraines are accumulations of till deposited at an ice margin, transverse to the local direction of ice-flow. The sediment comprising moraines can range in size from powdery silt to large boulders. A receding glacier can leave behind moraines that are visible long after the glacier retreats. Several different types of moraines can be recognized, but this study focuses on the few preserved in mountain valleys. A terminal (end) moraine marks the maximal or

outermost position of a glacier. The morphology of these moraines, are controlled by debris distribution on the surface and within the glacier. The type of landform that is generated, therefore, depends on two main variables, including the concentration of debris and the nature of debris supply (Glacial Geology: Ice Sheets and Landforms, Bennett and Glasser). Terminal moraines, specifically, consists of glacial debris that forms a ridge and is pushed forward by the snout of a glacier and is then deposited/dumped at the outermost edge of any given ice advance. This is due to the concentration of debris on the glacier surface being low. Terminal moraines typically have a curved shape and bulged appearance and may extend up the sides of lateral moraines. Recessional moraines are deposited upvalley of terminal moraines during pauses in glacial retreat or readvances of the glacier front. These deposits reveal the history of glacial retreats along the valley; in some instances, there can be five or more recessional moraines present in a glacial valley. The oldest moraines are downvalley and get progressively younger as the glacier changes positions and moves or retreats upvalley. Cosmogenic ^{10}Be surface exposure dating provides numeric ages and a complete chronology of moraines (Figure 4).

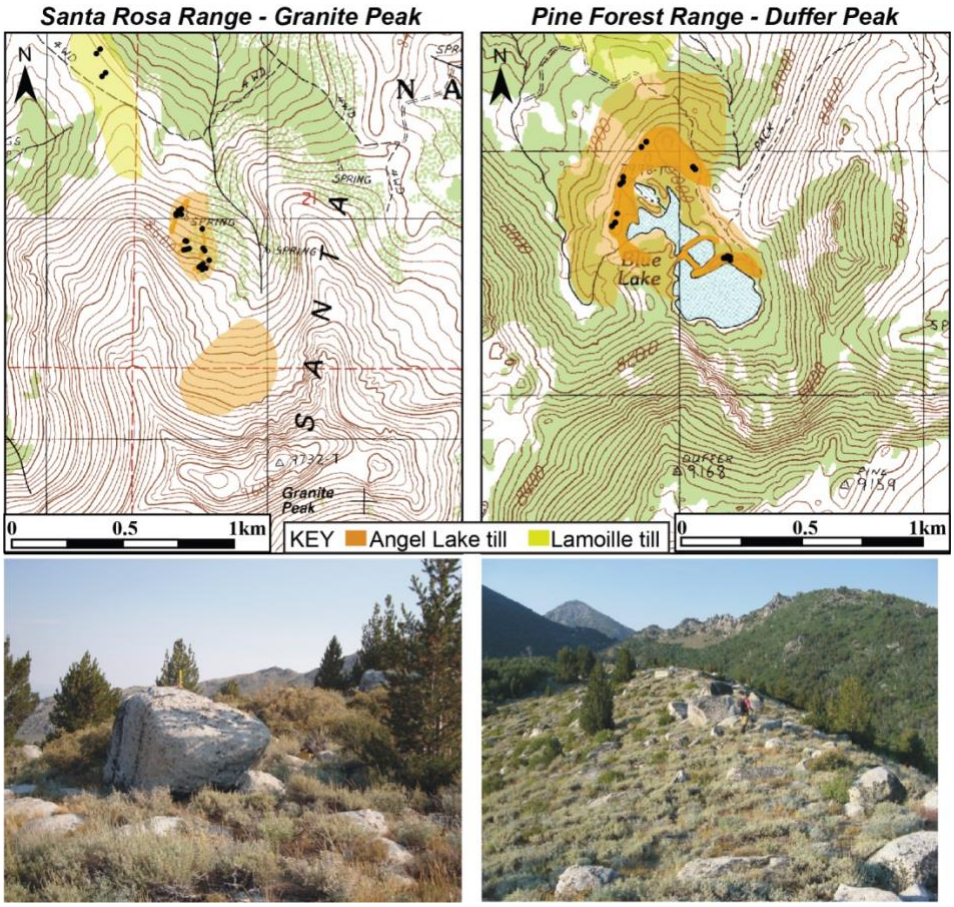

Figure 4. Upper two images represent mapped till and moraine crests (darkened areas) in key valleys of the Santa Rosa and Pine Forest Ranges. Black circles indicate locations of boulders sampled for cosmogenic ^{10}Be surface exposure dating. Lower two images represent actual images of boulders along with moraine crests taken out in the field by Dr. Jeff Munroe.

Glacial Erratics

Glacial erratics are large boulders or rocks that were glacially transported and then deposited at the glacier edge (Figure 5). Erratics can be carried and transported for many miles from their bedrock source and can range in size from pebbles to very large boulders. Erratics are identified by researchers studying the rocks surrounding the position of the erratic as well as the composition of the erratic itself. Erratics are quite significant because they help to determine the direction of past glacier movement and large erratic boulders atop moraines commonly used for cosmogenic ^{10}Be surface exposure dating. In order to use cosmogenic ^{10}Be surface exposure

dating, the erratics have to be composed in part by the mineral quartz. Quartz-rich, large erratic boulders are abundant atop moraines in the Santa Rosa and Pine Forest Ranges.

Figure 5. Image taken in the Pine Forest Range showing an example of a glacial erratic that is suitable for surface exposure dating (photo credit: Jeff Munroe).

CHAPTER 3: METHODS

Theory of Cosmogenic ^{10}Be Surface Exposure Dating

Cosmogenic nuclides are rare nuclides produced in rocks exposed at the Earth surface by the bombardment of cosmic-rays (Balco, 2011). Production rates of cosmogenic nuclides (in atoms per gram of rock per year) are greater at higher elevations due to the shielding effect of the atmosphere. The atmosphere reduces the energy of cosmic radiation, especially at low elevations where the atmospheric density is greatest. Areas at higher elevations have a thinner atmosphere above them, and therefore, the energy of cosmic radiation is greater. Nearly all production of the cosmogenic nuclides is by spallation reactions, which are reactions that are between primary or secondary cosmic-ray neutrons and elements present in surface materials. In addition, the concentration of cosmogenic-nuclide concentration in a rock sample is related to the length of time that the boulder or sample has been exposed at the surface of the Earth. Any event in which fresh rock has been brought to the surface can be dated by measuring the cosmogenic-nuclide concentration in the surface created by that event. The cosmogenic nuclide ^{10}Be is produced by spallation of O and Si in quartz.

Measurement of cosmic-ray produced nuclides in ^{10}Be involves a specific, energy-intensive analytical technique, accelerator mass spectrometry (AMS). The precision of AMS measurements depends on the efficiency of an ion source in converting the element of interest, such as ^{10}Be, into an ion beam accelerated and transmitted through the mass spectrometer and the precision of measuring the ion beam strength. The use of niobium metal powder as the binder with BeO has increased the efficiency of the ion source by a factor of 3-7 (Balco, 2011). The concentration of ^{10}Be is measured by an isotope dilution method in which a known amount of ^{9}Be carrier is added to the sample at the time of dissolution, the added ^{9}Be equilibrates with the

natural ^{10}Be released by dissolution, and then all Be is extracted from the solution and its isotope ratio is measured. The commercially available ^{9}Be carrier contains a small amount of ^{10}Be, which has a ^{10}Be/^{9}Be ratio near 10^{-15}. In order to have an accurate cosmogenic-nuclide exposure age, an accurate measurement of nuclide concentration and an accurate estimate of the nuclide production rate are needed.

Production of ^{10}Be in the mineral quartz occurs by high-energy spallation, negative muon capture, and fast muon interactions with silicon and oxygen (Balco, 2008). Only a single scaling scheme for nuclide production of muons is used. The production rates are calculated due to quick muon interactions according to Heisinger et al. (2002b), and due to negative muon capture according to Heisinger et al. (2002a.). Two things are required for the calculation of cosmogenic-nuclide production rates at a particular sample site: a scaling scheme that describes the variation of the production rate with time, location and elevation; and a reference production rate at a certain place and time. The reference production rate is determined by: (1) measuring the concentrations of nuclides in surfaces of known exposure age. This produces a set of local and time-averaged production rates. (2) Using the scaling scheme to scale these local, time-averaged production rates to the present time at sea level and high latitude and (3) averaging the reference production rates produce an estimate of the true value (Balco, 2008).

Cosmogenic ^{10}Be Exposure Dating of Moraines in the Santa Rosa and Pine Forest Ranges

This thesis provides the first cosmogenic chronology of glacial deposits in the Pine Forest and Santa Rosa Ranges based on new production and scaling models of *in situ* production of ^{10}Be. Seventeen samples, six samples from the Pine Forest Range and 11 samples from the Santa Rosa Range, were prepared in the Cosmogenic Nuclide Preparation Lab at NDSU following methods of Laabs and others (2013). The samples were sent to PRIME Lab at Purdue University

for $^{10}Be/^{9}Be$ measurement by AMS. We calculated cosmogenic ^{10}Be surface exposure ages of terminal moraines of the last glaciation using the calibrated *in situ* production rate for ^{10}Be determined at Promontory Point, Utah, with the LSDn production scaling model of Lifton and others (2014) as implemented in version 3.0 of the University of Washington online exposure age calculator (Balco and others, 2008; http://hess.ess.washington.edu).

In order to calculate an exposure age or erosion rate for cosmogenic ^{10}Be surface exposure dating, the following inputs are needed: Sample name, latitude, longitude, elevation, sample thickness, sample density, shielding correction, erosion rate, nuclide concentrations, and uncertainties in nuclide concentrations. The elevation can be specified either as meters above sea level or as mean atmospheric pressure at the site. The shielding correction is the ratio of the production rate at the obstructed site to the production rate at a site at the same location and elevation, but with a flat surface and a clear horizon (Balco et al. 2008). The nuclide concentrations accounts for laboratory process and carrier blanks. They are referred to as the ^{10}Be concentrations in quartz in the sample. The uncertainties in the nuclide concentrations are 1 standard error analytical uncertainties in the measured nuclide concentration and account for all sources of analytical error (Balco et al. 2008).

Glacier Modeling Procedure

Glacial chronologies, by themselves, are not a direct indicator of climates accompanying intervals of known ice extent. This study also uses a forward numerical modeling approach to determine climate conditions, in terms of temperature and precipitation, that accompanied the known maximum ice extents for the last glaciation in the Santa Rosa and Pine Forest Ranges. The coupled energy-mass balance and ice-flow models used in this study were originally developed by Plummer and Phillips (2003) and have been used to estimate paleo-climate

conditions for paleo-glaciers in various mountain glacier settings (Rowan et al., 2014; Harrison et al., 2014; Leonard et al., 2017). The modeling approach aims to match simulated ice extents produced under specific paleoclimate conditions (e.g., temperature depression from modern and precipitation) to known ice extents reconstructed from glacial deposits and landforms identified in the field (e.g., terminal and lateral moraines). The modeling approach consists of two numerical models, a mass and energy balance model and an ice flow model. The energy-mass balance model calculates monthly snow accumulation and ablation at every cell within the model domain, a gridded digital elevation model of a glacial valley, for the time interval of interest (Figure 6).

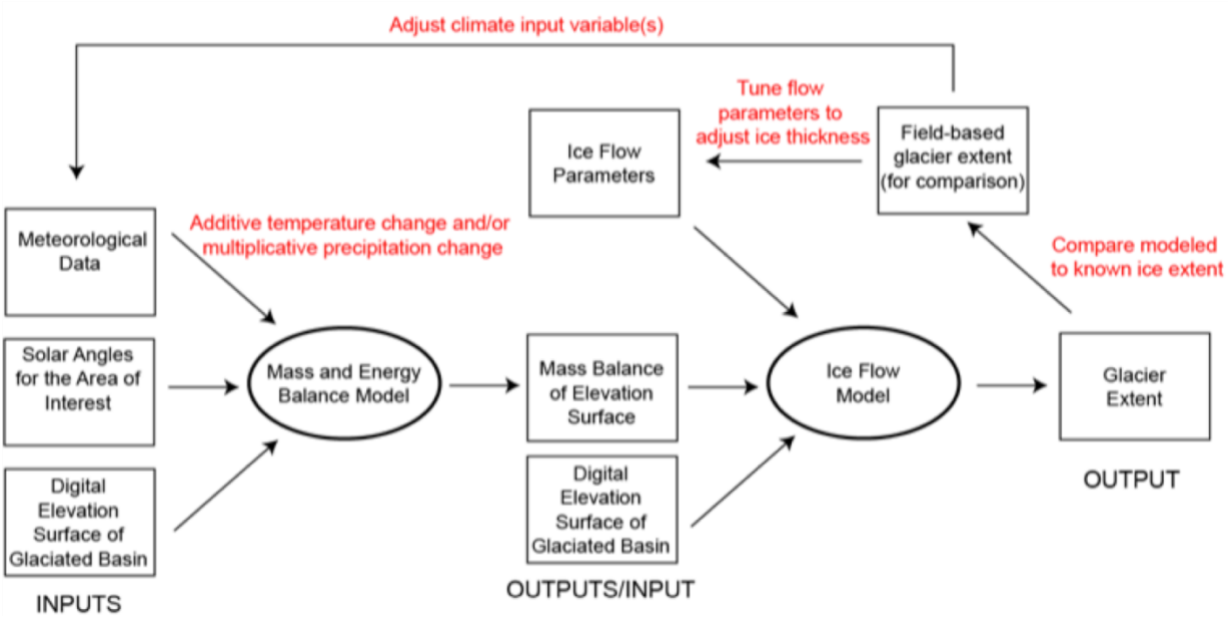

Figure 6. Flow diagram indicating inputs and outputs for a two-dimensional mass balance and ice-flow model to predict temperature and precipitation combinations to reconstruct glaciers at a known extent.

The mass and energy balance model computes monthly mass balance through the northern hemisphere water year, starting in October and ending in September. Annual mass balance depends mostly on precipitation and temperature, which are the primary inputs to the

model (Plummer and Phillips, 2003). The other inputs for the mass and energy balance model include secondary meteorological data, solar angles for the area of interest, and a digital elevation surface of the glaciated basin. Average monthly cloudiness and relative humidity are held constant at every cell and elevation within the model domain (Plummer and Phillips, 2003). The source of the inputs, including windspeed, cloudiness, and relative humidity come from RAWS (remote automated weather station). Temperature and precipitation inputs, on the other hand, are derived from gridded models for the model domain produced by the PRISM climate group from Oregon State University, (http://www.prism.oregonstate.edu). For each grid cell, PRISM calculates a climate-elevation regression, and stations entering the regression are assigned weights based on the physiographic similarity of the station to the grid cell (Daly et al. 2007). The factors considered are elevation, location, topographic facet orientation, etc. Additionally, the data from the stations were spatially quality controlled and short-period-of-record averages were adjusted in order to better emulate the 1971-2000 period (Daly et al. 2007).

Sublimation and monthly snow losses due to melting are calculated from the surface energy balance. The total is calculated only during melt season. During the winter months, only the energy transfer associated with sublimation is calculated. Solar angles are calculated according to standard methods except that secular variations in solar angles and Earth-sun distance so that the effect of Milankovitch climatic controls can be included (Plummer and Phillips, 2003). In order to get a net annual mass balance, the monthly mass balance is summed through the water year. To simulate a climate under which Pleistocene glaciers could have existed at steady state, the modern temperature and/or precipitation are deviated to simulate a paleo-mass balance under colder and/or wetter climate compared to modern. The output is a net

annual mass balance defining the areas of net accumulation and net ablation in the model domain, which is used as an input for the ice flow model.

The ice flow model calculates the time-dependent flux of ice into or out of each cell in a grid from a set of finite difference equations relating to flow thickness, surface-slope and bed-slope (Plummer and Phillips, 2003). When applying the ice flow model to the study of geomorphic features of glaciers, we assume that major moraines represent a temporary steady-state condition. Even though the ice flow model describes transient glacier response, we are only considering steady-state solutions. The primary variable in the model calculations is ice-free surface elevation, the behavior of which is not constant across the grid. Ice surface elevation can either increase or decrease in ice-covered portions of the grid, but can only increase or remain constant in ice-free areas (Plummer and Phillips, 2003). The output of the ice flow model is a gridded glacier extent, which can be compared to the modeled or known ice extent. The trial-and-error method of calculating glacier mass balance based on an estimated temperature and precipitation combination and forward modeling of the glacier extent based on mass balance allows us to compare the glacier modeling results with the known ice extent. This ultimately produces a set of temperature and precipitation combinations that could have accompanied the glacier at steady state.

Lake Modeling Procedure

Glacier modeling is not a direct indicator of climates at known intervals, but if we compare glacier modeling results with the results that we generate from lake modeling, we will be able to interpret climate. This study also uses the water balance modeling methods of Condom et al. (2004). The water balance modeling methods were applied to Lake Franklin in order to limit the range of temperature and precipitation combinations accompanying lake highstands that

overlap in time with periods of moraine deposition in the Ruby Mountains. This method is advantageous because it uses locally calibrated monthly evaporation rates and a soil water storage parameter for closed-basin lakes (Figure 7). These calibrations are possible in the Lake Franklin basin as well as other nearby pluvial lake basins because of the available monthly pan evaporation data from the Western Regional Climate Center (www.wrcc.dri.edu/) and total solar radiation data from a National Renewable Energy Laboratory site in nearby Elko, Nevada, (http://rredc.nrel.gov/solar/old_data/nsrdb/). The hydrologic balance modeling methods used in this study were originally developed by Condom et al. (2004) and have been used to estimate paleo-climate conditions for pluvial lakes in high altitude desert settings in South America.

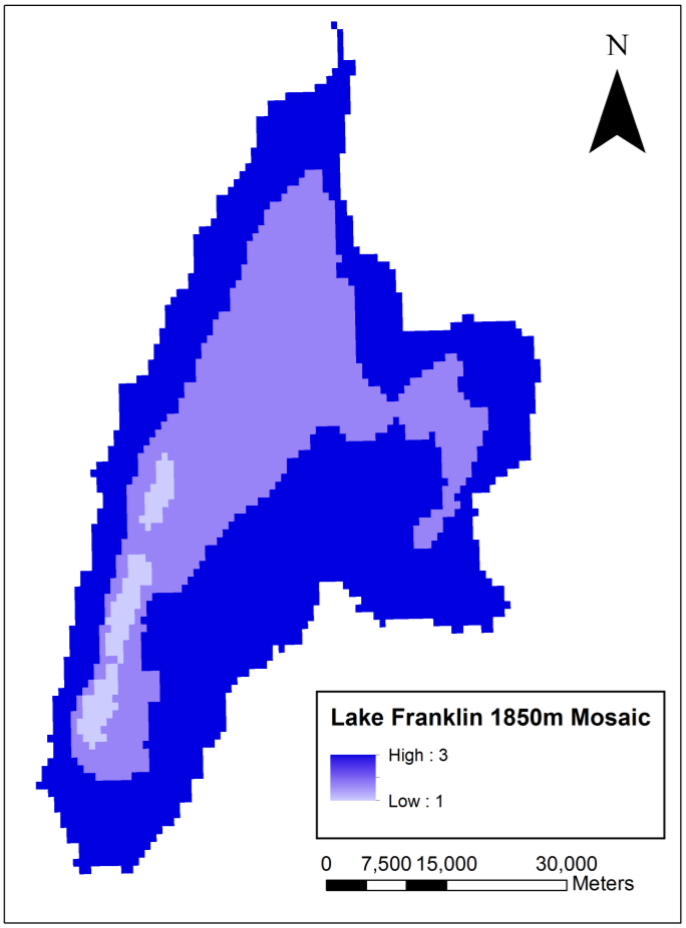

Figure 7. An example of grid-based modeling, this figure representing a mosaic file for Lake Franklin.

Evaporation Calibration

The only validation of the lake model is the evaporation calibration. The water balance modeling approach has many challenges, but the one that is most prominent, is developing an expression to account for potential evaporation. Potential evaporation is defined as the amount of evaporation, based on the available energy for evaporation, that would exist at Earth's surface. A study was conducted by Steen et al. (2015), which focused on a simplified method that focused on the energy driven component of evaporation, which as stated previously, can be calibrated based on the available modern monthly pan evaporation data near the Lake Franklin watershed. More specifically, Steen et al. (2015) looked at testing a number of expressions in order to simulate measured Ruby Lake pan evaporation from the Western Regional Climate Center (WRCC). Four expressions were deemed to be the most applicable for computing potential evaporation (Steen and others, 2015). The meteorological variables for the four expressions were determined from measurements of average solar radiation, temperature, and relative humidity in Elko, NV. Estimated sunshine hours per day were also used as a variable. The following equation, taken from Condom et al. (2004), was used to model potential evaporation within two subcatchments of the Andean Altiplano:

$$EP = \frac{Rg}{\lambda}(T + 17.8) * 0.0145$$

EP is evaporation (mm/day), Rg is the total solar radiation (in J/cm^2/day), T is the mid-month air temperature (°C), and λ is latent heat (Cal/g); (Steen and others, 2015). Other equations were also looked at, but the equation taken from Condom et al. (2004) was used for this thesis study. Because evaporation is estimated for an open water surface, the evapotranspiration and evaporation are considered to be interchangeable for the above equation. For the above equation,

meteorological data were applied for each month of the year, and was then compared to the actual pan evaporation data to obtain the best viable calibration (Steen and others, 2015).

In order to use the equation for the Lake Franklin watershed rather than for Lake Titicaca and the Tauca paleolake of the Andean Altiplano, an alteration of the coefficient 0.0145 to 0.0382 was used to yield the final equation:

$$EP = \frac{Rg}{\lambda}(T + 17.8) * 0.0382$$

The final step for calibrating the potential evaporation, includes modifying the Rg portion of the equation, using incoming solar radiation as computed by the Plummer and Phillips (2003) mass and energy balance model, which yields the following equation:

$$\frac{Rg}{Re} = a + b\left(\frac{Sun_{tr}}{Sun_{th}}\right)$$

The solar radiation output from the Plummer and Phillips (2003) model and the extended Rg term, as well as the modified Condom et al. (2004) equation remains an accurate model for potential evaporation as well as an accurate validation of the lake model (Steen and others, 2015).

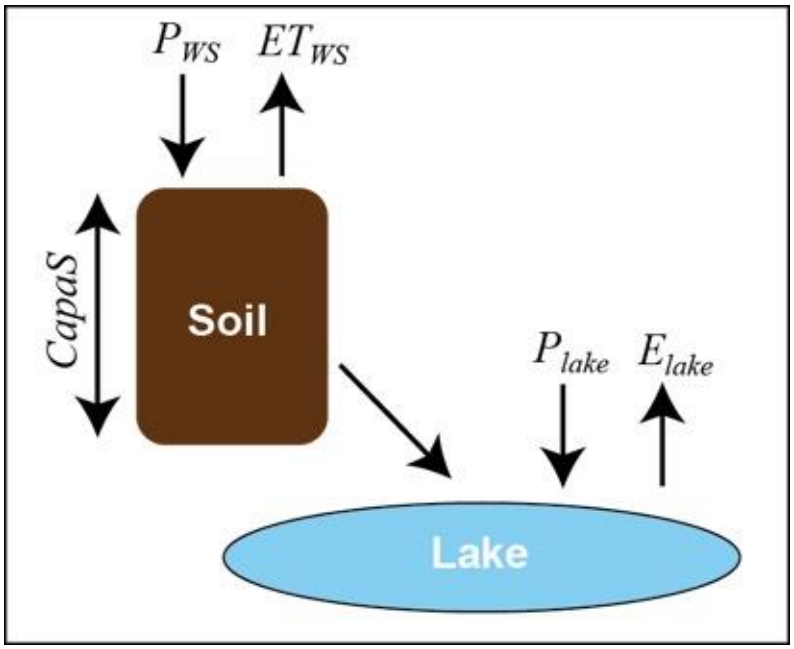

Figure 8. Flow diagram indicating the inputs necessary for the water balance model.

The modeling approach aims to calculate the monthly changes in the volume of a lake. The modeling approach consists of two reservoirs: the soil (or watershed) and the lake (Figure 8). Depending on the water balance in the two reservoirs, the surface area may change at each time step. As the soil recharges the lake, the two reservoirs are connected. The primary inputs are precipitation on the watershed (P_{ws}), evapotranspiration from the watershed (ET_{ws}), precipitation on the lake surface (P_{lake}), and evaporation from the lake surface (EP_{lake}). Monthly precipitation and temperature gridded values were obtained for the Lake Franklin watershed from the PRISM Climate Group of Oregon State University (2004); (Figures 9 and 10). The temperature for every point in the watershed, which is represented as an 800 m gridded domain, are necessary as part of the calculation of potential evaporation by the equation taken from Condom et al. (2004), (Steen, 2015). The equation was originally developed for evaporation on the Andean Altiplano, but was later modified to yield the calibrated expression used for Lake Franklin.

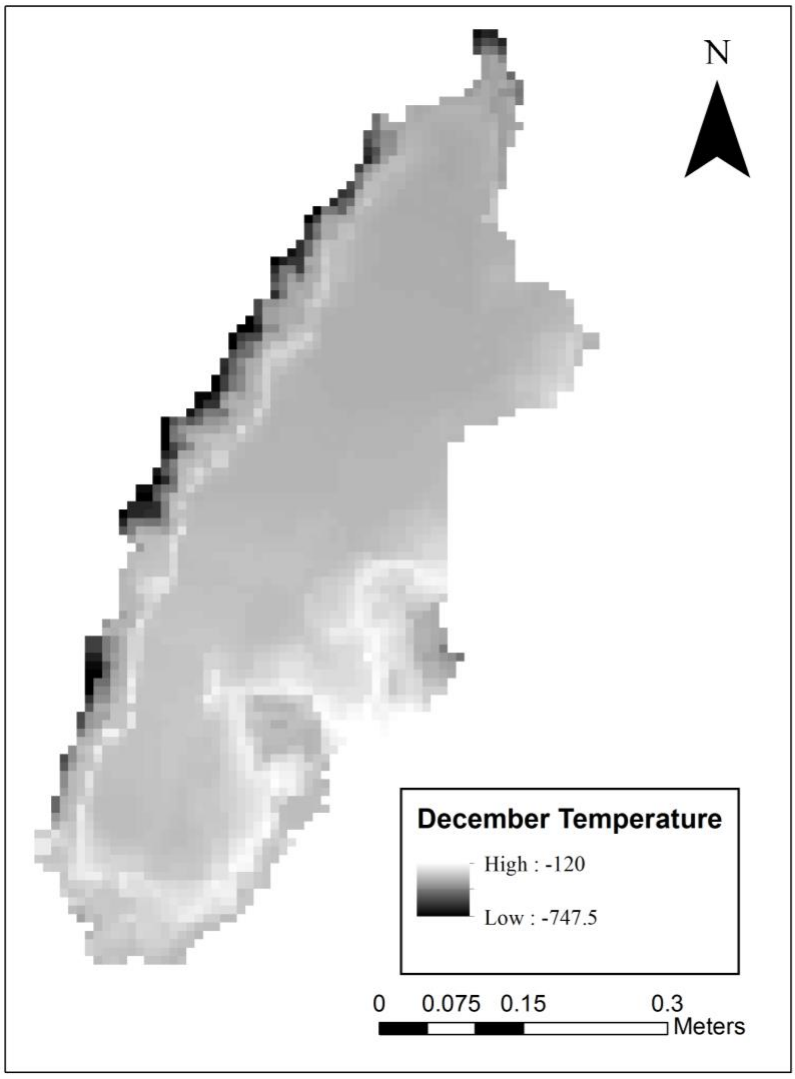

Figure 9. An example of grid-based modeling, this figure representing a temperature input grid file for the month of December used for modern Lake Franklin. The temperature is multiplied by 100.

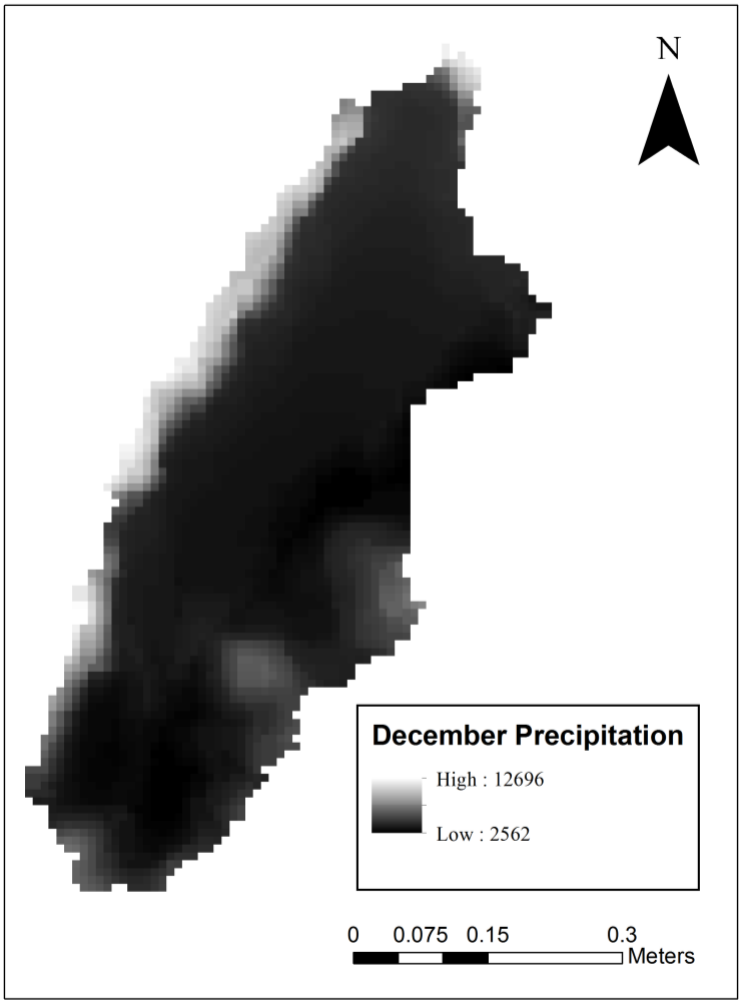

Figure 10. An example of grid-based modeling, this figure representing a precipitation input grid file for the month of December used for modern Lake Franklin. The precipitation is multiplied by 100.

The Lake Franklin watershed is a closed basin. Because of this, no discharge term is necessary in the water balance equation. The equation below (modified from Condom et al., 2004) is used to calculate changes in the volume of a closed basin lake:

$$\frac{dV_{lake}}{dt} = (P_{lake} - Ep_{lake})A_{lake} + (P_{ws} - Et_{ws})A_{ws}$$

Where A_{lake} is the lake's surface area, and A_{ws} is the watershed's surface area. Typically, this expression requires a runoff coefficient to be multiplied by the watershed (ws), but previous studies have suggested that the estimation of a runoff coefficient (k) can bey very difficult. This

is can be due to the fact that there is high variability in this value as a result of runoff diversions, irrigation, groundwater discharge differences, and inconsistency in rainfall events near rivers (Prudic et al., 2005), all of which exist in valleys of the Great Basin.

To avoid the challenges and uncertainties of estimating a runoff coefficient, a soil-water reservoir within the Lake Franklin basin was computed instead in the water balance model following the methods of Condom et al. (2004). The *CapaS* parameter, which is the soil water capacity for each cell in the watershed, was calibrated based on the pre-diversion extents of the modern lake at the southern end of the Lake Franklin basin. *CapaS* was calculated as the surplus water that can be stored in a soil reservoir when the lake reservoir is filled. This was done by determining how much runoff from precipitation is necessary to sustain the lake. This method is advantageous to hydrologic modeling because it requires only two water reservoirs, the lake and soil, as well as the *CapaS* parameter. This method also removes the need for a runoff coefficient as well as accounting for ground water fluxes.

When the model calculates *CapaS*, another value, H_{ws}, which is the actual water content of the soil reservoir is calculated too. In order for the calculation to start, H_{ws} must be set to an initial value. For example, if soil water content exceeds soil water capacity after the calculation is run over a certain period of time, then potential evapotranspiration from the watershed (Etws) is calculated using the calibrated potential evaporation equation (Condom et al., 2004; Steen, 2015). The equations shown below and taken from Condom et al. (2004) are solved iteratively to produce CapaS for the Lake Franklin watershed:

$$Etws_{n+1} = \left(\frac{Hws_n}{\text{CapaS}}\right) \times \left(2 - \frac{Hws_n}{\text{CapaS}}\right) X\ EP_{n+1}$$

$$Hws_{n+1} = Hws_n + Pws_{n+1} + Etws_{n+1}$$

The model was run entirely through the MATLAB program. In order to compute *CapaS* values for the modern lake watershed, gridded inputs, including mean monthly precipitation, temperature, and solar radiation data as well as a gridded raster representing the lake watershed coded for the modern lake, paleolake, and the area outside the lake were compiled. *CapaS* for the modern watershed was assumed to be the same for the pluvial lake watershed. We do this because the surficial geology and vegetation did not change from the Pleistocene to the modern, but this assumes that any excess precipitation accompanying the paleolake Franklin runs off into the lake. For this study, only the maximum and minimum *CapaS* values were used. Two *CapaS* values were used because the modern lake is somewhat complicated by the fact that it changes in size and that some diversions of water in the northern basin reduce runoff toward the modern lake. Once the two *CapaS* values were obtained, they were then used as inputs into the second part of the modeling, which was the modeling of paleo-lake Franklin. The only change in inputs for the second part of the modeling, simulation of temperature and precipitation conditions accompanying the Lake Franklin highstands, were the temperature grids. Temperature grids of 0° (representing modern conditions), -2.5°, -5°, -7.5°, -10°, and -12.5° Celsius were used in simulations of different shoreline elevations of Lake Franklin highstands. Two reconstructed shoreline elevations of 1830 m, representing the shoreline of Lake Franklin during the late Last Glacial Maximum, and 1850 m, representing the shoreline of Lake Franklin at 17 ka was used for this model. These two reconstructions of Lake Franklin were determined by Munroe and Laabs (2013) based on radiocarbon dates of shoreline deposits. For the paleolake calculation, the inputs required were the modern *CapaS* value and the months that the watershed and lake were frozen, which varied depending on the temperature grid used. For example, there were only four months in which both the watershed and the lake were frozen for the -2.5-temperature grid,

whereas there were eight months for the -12.5-temperature grid. This step of the model calculation uses the modern *CapaS* and solves for the factor by which precipitation would have to be multiplied to sustain the lake. The outputs for this script were then used to compare against the glacier modeling results in order to identify overlapping temperature and precipitation combinations.

CHAPTER 4: RESULTS AND DISCUSSION

Cosmogenic ^{10}Be Surface Exposure Dating Results

Four cosmogenic ^{10}Be exposure ages from a terminal moraine in the Pine Forest Range span 19.9 ± 0.5 ka to 21.2 ± 0.6 ka, coinciding with the latter part of the Last Glacial Maximum. An exposure age of 32.0 ± 0.7 ka from the same terminal moraine is significantly older than the other exposure ages, which indicates that the boulder was exposed for a period of time ~50% longer than the other four cosmogenic exposure ages (Figure 11). This could be explained by a period of surface exposure predating deposition of the rest of the moraine. For example, the rock could have been exposed on the face of a nearby cliff and then fell upon the glacier surface before being deposited. Because of its older exposure age, this sample is not included in the calculation of a mean exposure age of the moraine. A single exposure age of 17.6 ± 0.5 ka on a younger moraine upvalley of the terminal moraine represents the time of a later advance or pause in ice retreat, although additional cosmogenic exposure ages are needed to obtain an accurate numeric age of this moraine (Figure 11).

Five cosmogenic ^{10}Be surface exposure ages from a terminal moraine in the Santa Rosa Range span 16.8 ± 0.6 ka to 18.7 ± 0.9 ka, coinciding with the earlier part of Heinrich Stadial 1. These results indicate that glaciers in the Santa Rosa Range were at their maximum extent. Further upvalley, six exposure ages from recessional moraines are slightly younger and range from 15.2 ± 0.5 ka to 17.0 ± 0.8 ka (Figure 12). These younger moraines upvalley suggest that ice readvanced to, or persisted within, 90% of its maximum length after the terminal moraine was abandoned ca. 18.3 ± 0.9 ka. The ages of the moraines in both the Santa Rosa and Pine Forest Range can be compared against other glacial chronologies in the Great Basin.

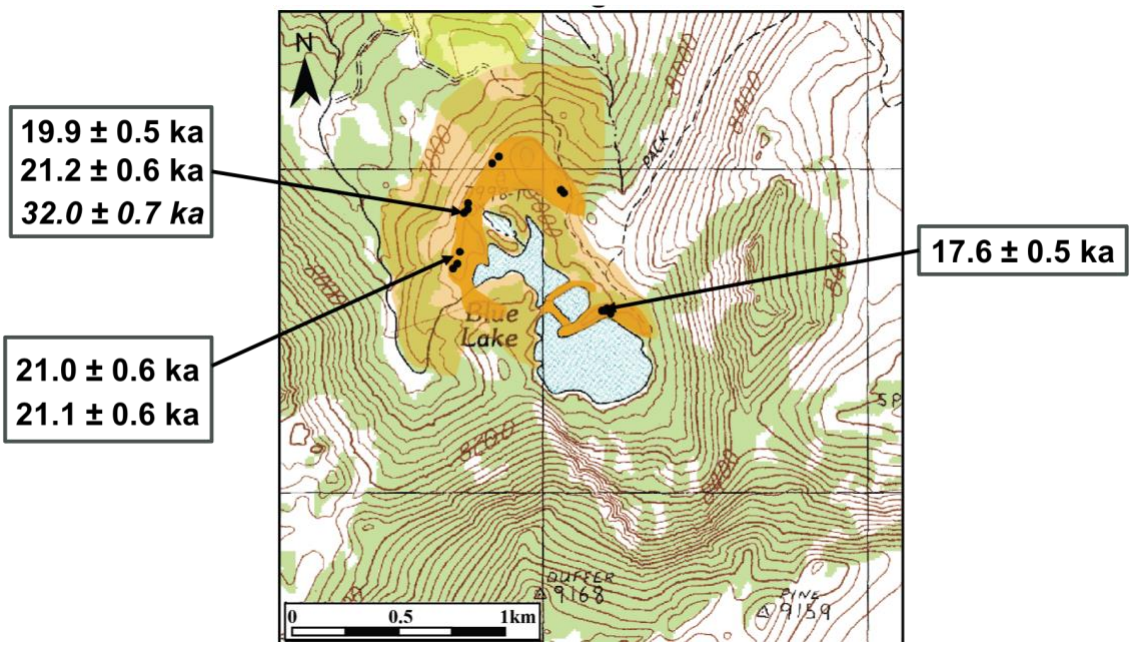

Figure 11. Mapped till and moraine crests (darkened areas) in key valleys of Pine Forest Range. Black circles indicate locations of boulders sampled for cosmogenic ^{10}Be surface exposure dating. The two boxes to the left contain cosmogenic ages for the terminal moraine. The box to the right contains one cosmogenic age for the recessional moraine.

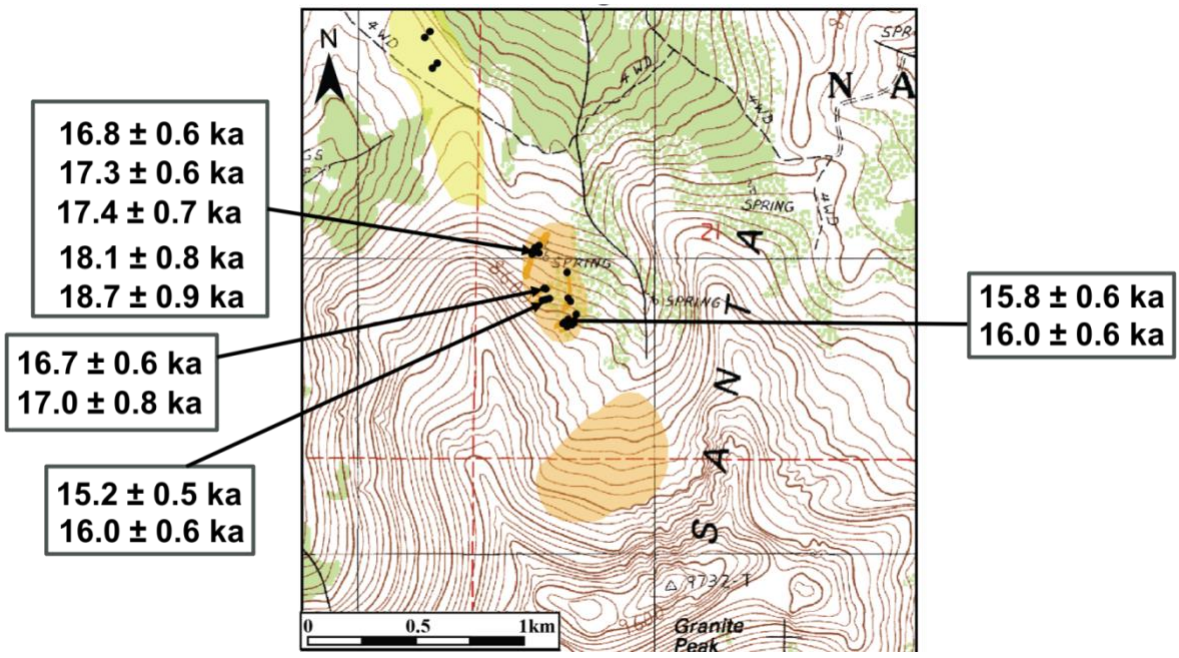

Figure 12. Mapped till and moraine crests (darkened areas) in key valleys of Santa Rosa Range. Black circles indicate locations of boulders sampled for cosmogenic ^{10}Be surface exposure dating. The upper box to the left contains cosmogenic ages for the terminal moraine. The lower boxes and the box to the right contains cosmogenic ages for the recessional moraines.

Cosmogenic ^{10}Be Surface Exposure Dating Discussion

Resolving mountain glacier chronologies from the Last Glacial Maximum (21-20 ka) through the 18-17 ka interval in the Pine Forest and Santa Rosa Ranges, respectively has implications for understanding Late Pleistocene climate conditions. This is true across the northern Great Basin and elsewhere in the western United States. The chronology of glacial deposits in the northcentral Great Basin, specifically in the Ruby Mountains reveals an average terminal moraine age of 20.9 ± 1.2 ka compared to one recessional moraine that had an average age of 17.2 ± 1.0 ka for Seitz Canyon. Overland Creek, also located in the Ruby Mountains reveals an average terminal age of 19.9 ± 1.0 ka and an average recessional age of 16.2 ± 0.8 ka. In the East Humboldt Mountains, an average recessional moraine age of 17.4 ± 0.5 ka for Angel Lake was revealed. In the northeastern Great Basin, chronologies were similar, more specifically in the Wasatch and Uinta mountains.

Alongside recent work in the Wasatch Range Mill B left lateral moraine (20.2 ± 1.1 ka; Quirk et al. 2018), we have identified a terminal moraine in the Pine Forest Range with mean exposure ages broadly consistent with global Last Glacial Maximum. In the Wasatch, the exposure ages from Quirk et al. (2018) strongly suggest that glaciers reached stable moraine building maxima prior to the highstand of Lake Bonneville. In the Pine Forest Range, moraine ages also suggest that glaciers reached their maximum extents prior to the highstand of Lake Franklin and Lake Surprise. These moraine ages across the northern Great Basin suggest that glaciers were at their maximum extents during the latter part of the LGM (21-20 ka) while most Great Basin lakes were below the level of their highstand shorelines. Additionally, alongside recent work in the Wasatch Range, the Solitude moraine (15.5 ± 0.8 ka; Quirk et al. 2018), we have identified a terminal moraine as well as younger moraines upvalley in the Santa Rosa

Range with mean exposure ages broadly consistent with the 18-17 ka time interval. These ages suggest that the stadial represented by the Solitude moraines in the Wasatch Range as well as the moraines in the Santa Rosa Range may be coincident with the early part of Heinrich Stadial 1 (HS1; spanning 18.0-14.5 ka; Hemming, 2004). In mountains of the northcentral and northeastern Great Basin, cosmogenic ^{10}Be exposure dating of multiple moraine complexes indicate that glaciers were within 75-100% of their maximum lengths both before and during highstands of paleolakes in northern Utah and Nevada (Laabs and Munroe, 2016). This suggests that mountain glaciers located throughout the Great Basin either persisted or readvanced to near-maximum extents during lake highstands while global ice volume was declining (Figure 13).

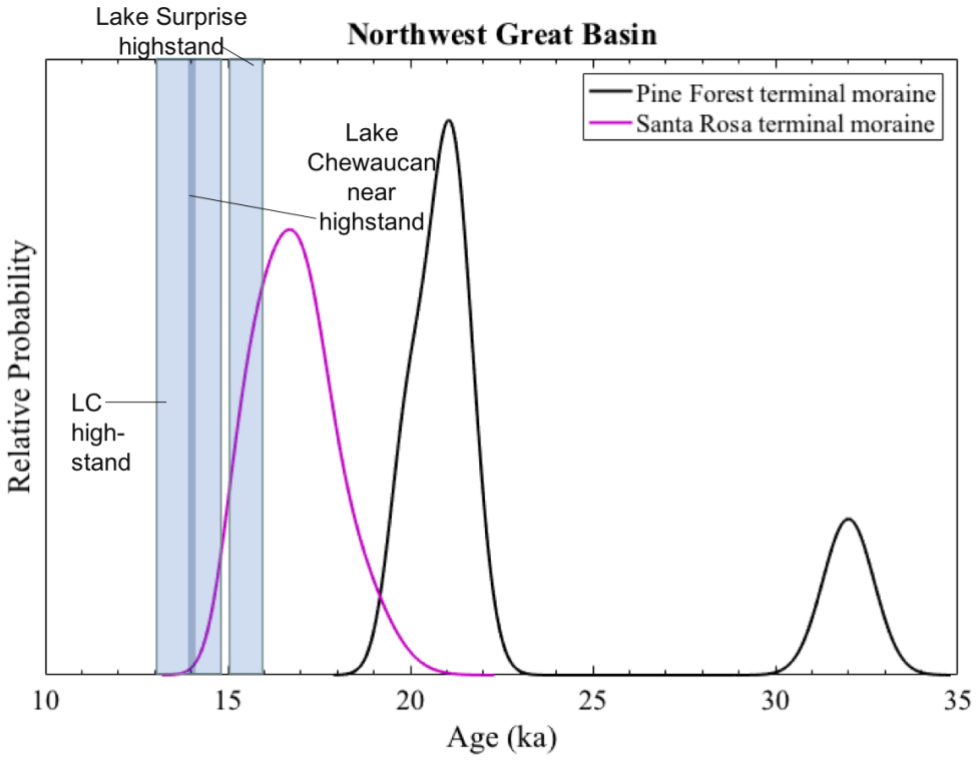

Figure 13. Relative probability plot of cosmogenic ^{10}Be exposure ages in the northwest Great Basin, including the Pine Forest and Santa Rosa Ranges. Ages are shown relative to the Lake Surprise and lake Chewaucan near highstands and highstands.

Other studies of glacial chronologies in the western United States have provided more insight for the timing of the last glaciation. For example, Phillips et al. (2016) looked at securing glacial chronology of late Pleistocene moraines in the Sierra Nevada. This was done by using direct radiocarbon ages marking glacial termini at various times and by chronologies of lacustrine sediment cores, marine sediment cores, and speleothem calcite, which provided evidence for the timing of glacial fluctuations (Phillips et al. 2016). The Tioga Glaciation, the last Pleistocene glaciation in the Sierra Nevada, has been subdivided into multiple episodes. From >20 ka to ~17 ka, Tioga 3 glaciers were close their maximum extent (Phillips et al. 2016). Glaciers retreated rapidly at ~17 ka and then began to readvance at ~16.8 ka. At ~16.2 ka, the Tioga 4 readvance culminated and rapid retreat followed, with the equilibrium line altitude rising by 400 m by ~15.7 ka (Phillips et al. 2016) and the range most likely became ice-free by a short time thereafter. Tioga 3 is identified by Phillips et al. 2016 as equivalent to the LGM, and Tioga 4 is a readvance equivalent to the ~17 ka signal that we are seeing in the Great Basin. We do not subdivide the Angel Lake Glaciation into episodes here, but the numerical ages of terminal and recessional moraines of the Angel Lake Glaciation and Tioga 3 and 4 Glaciations are aligned (Figure 14). From 21-20 ka and 18-17 ka, Pine Forest and Santa Rosa glaciers were also close to their maximum extent. Additionally, results from younger moraines upvalley from the Santa Rosa Range are comparable with results from Phillips et al. (2016) in which the glaciers either readvanced to, or persisted within, 90% of its maximum length after the terminal moraine was abandoned.

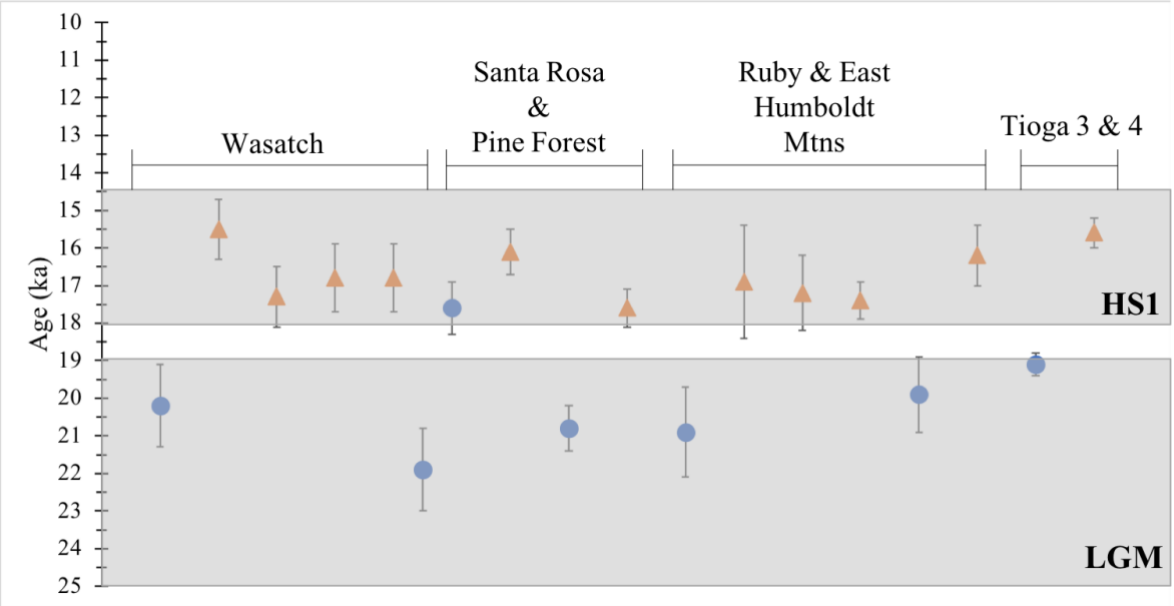

Figure 14. Mean ^{10}Be surface exposure ages taken from ranges across the northern Great Basin and western United States corresponding to HS1 and the LGM. Circles represent terminal moraines whereas triangles represent recessional moraines. Mean ^{10}Be surface exposure ages for the Wasatch, Ruby and East Humboldt Mountains and Tioga 3 and 4 were taken from Quirk et al. 2018 and Laabs and Munroe, 2016, Munroe et al. 2015 and Laabs and Munroe et al., 2013, and Phillips et al. 2017, respectively.

Glacier and Lake Modeling Results for the Northwest and Northcentral Great Basin

Cosmogenic surface exposure ages provide the chronological framework for interpreting results of glacier modeling experiments in the two mountain ranges. The glacier modeling outputs for both the Santa Rosa and Pine Forest Range show that the modeled glacier shapes closely match the small, simple shapes that characterize the known ice extents (Figures 15-17). The Santa Rosa and Pine Forest model results include a broad range of temperature and precipitation combinations that could have accompanied glacier maxima in the two mountain ranges. For example, if precipitation in the Pine Forest Range was similar to modern at the time of the local glacial maximum (~21-20 ka), then temperature depressions during the last glaciation were -9 to -8°C. If precipitation in the Santa Rosa Range was similar to modern during the later glacial maximum at ~18-17 ka, then the temperature ranges were -6 to -5°C. If

temperature depressions were greater or less than this, then accompanying precipitation rates would have been less/greater than modern.

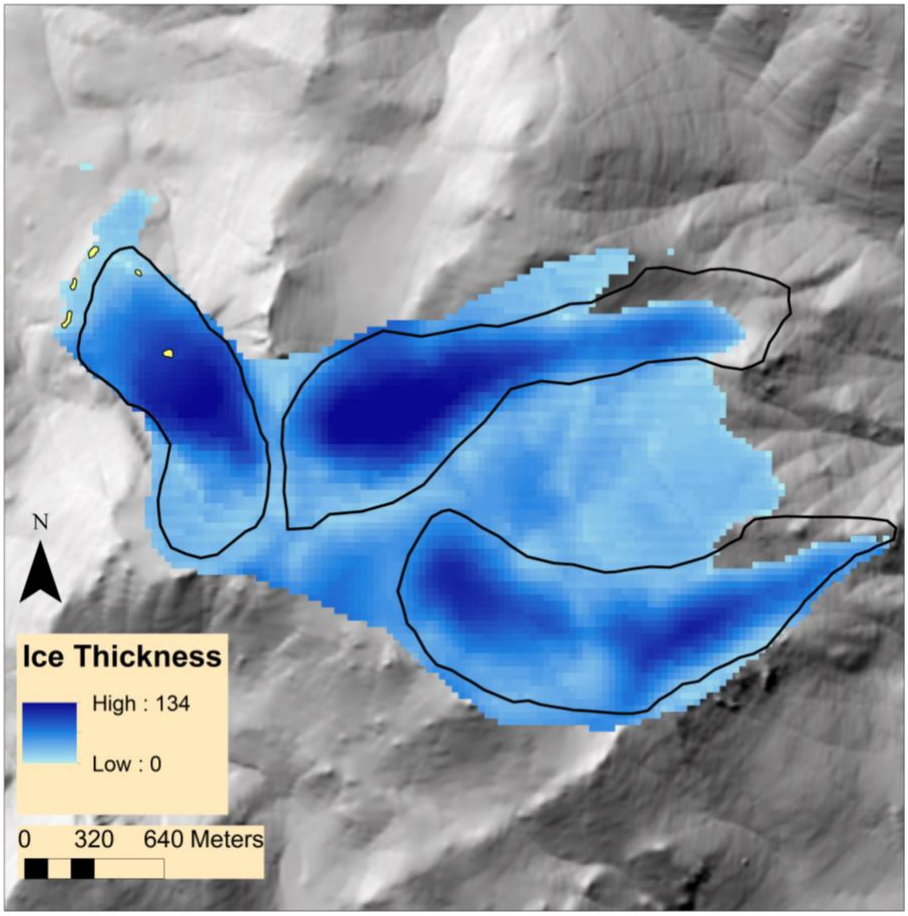

Figure 15. The reconstructed ice extents (black outline) and the modeled ice extents are shown for the terminal moraine (yellow dots) of the Pine Forest Range, Nevada. The temperature-precipitation combination used for this modeled output was T-9.1°C, Px1.

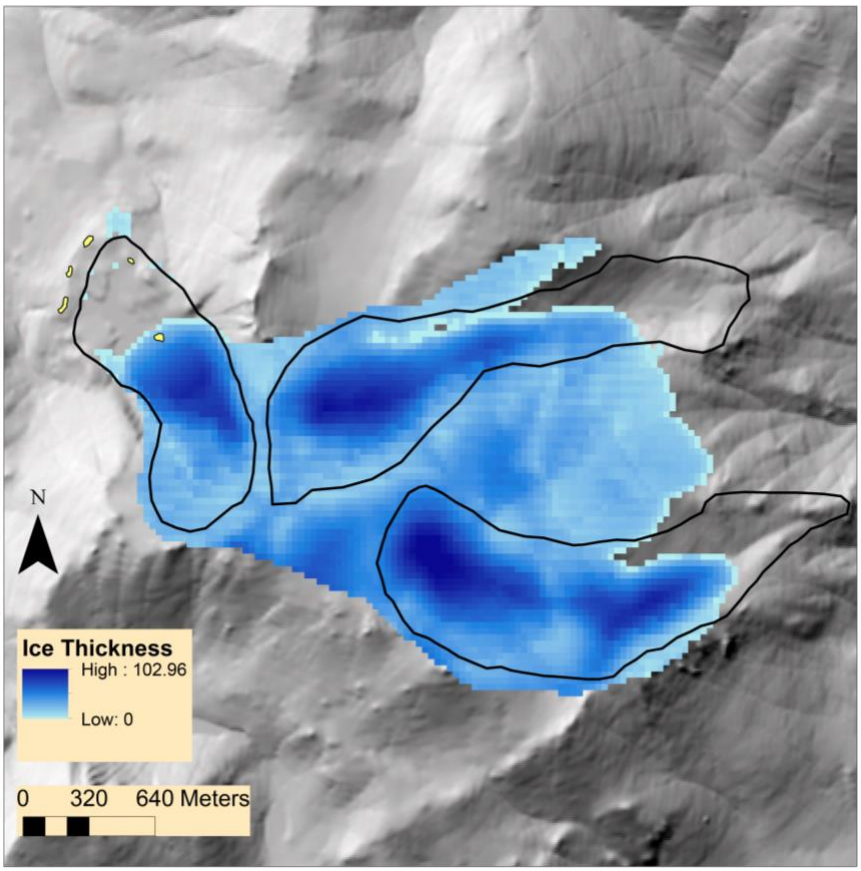

Figure 16. The reconstructed ice extents (black outline) and the modeled ice extents are shown for the recessional moraine (yellow dots) of the Pine Forest Range, Nevada. The temperature-precipitation combination used for this modeled output was T-8.7°C, Px1.

The glacier modeling results for the 21-20 ka interval for the Pine Forest terminal moraine show that the modeled glacier shapes closely match the small, simple shapes that characterize the known ice extents (Figure 15). The glacier modeling results reveal a range of temperature and precipitation combinations that accompany the Pine Forest terminal moraine. Temperature and precipitation combinations include deviated temperatures ranging from -10.4 to -7.15 and precipitation factors that range from 0.5 to 2 (appendix C). The glacier modeling results for the 21-20 ka interval for the Pine Forest recessional moraine also shows that the modeled glacier shapes closely match the known/mapped ice extent (Figure 16). Temperature and precipitation combinations for the Pine Forest recessional moraine include deviated

temperatures ranging from -10 to -6.7 and precipitation factors that range from 0.5 to 2 (appendix C).

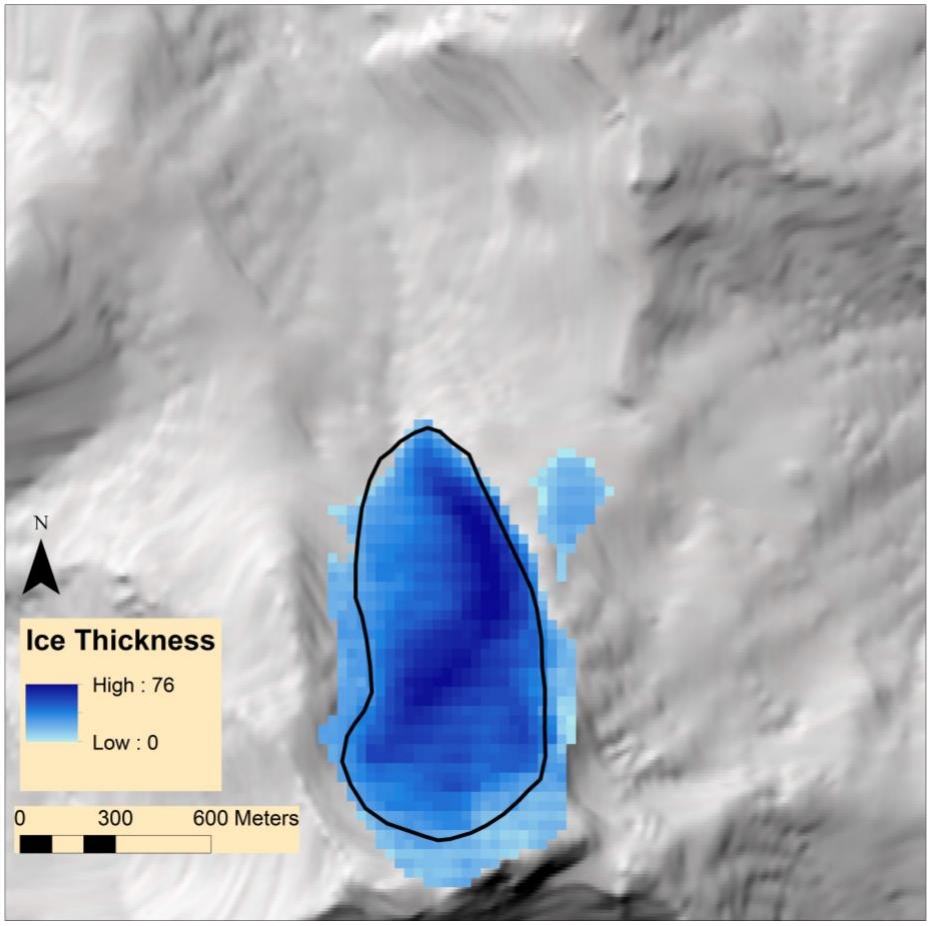

Figure 17. The reconstructed ice extent (black outline) and the modeled ice extent is shown for the terminal moraine of the Santa Rosa Range, Nevada. The temperature-precipitation combination used for this modeled output was T-6.1°C, Px1.

The glacier modeling results for the 18-17 ka interval for the Santa Rosa terminal moraine show that the modeled glacier shapes closely match the small, simple shape of the known ice extent (Figure 17). The glacier modeling results reveal a range of temperature and precipitation combinations that accompany the Santa Rosa terminal moraine. Temperature and precipitation combinations include deviated temperatures ranging from -8.05 to -4.35 and precipitation factors that range from 0.5 to 2 (appendix C).

It is difficult to identify a unique temperature and precipitation combination for the time intervals 21-20 ka and 18-17 ka when considering only glacier modeling results (Figures 18 and 19). We compare modeling results reported here with others from the northern Great Basin and results of water budget modeling studies of pluvial lakes to identify a unique temperature and precipitation combination for a given time interval. Glacier modeling results are available for the eastern Ruby Mountains (Overland Creek valley; Reimers et al. 2016) and the western Ruby Mountains (Seitz and Hennen Canyons; Truong et al., 2014) as well as the Angel Lake valley in the East Humboldt Mountains (Bradley et al. 2015), (Figure 1), providing additional limits on possible temperature and precipitation combinations for the time interval 18-17ka and 21-20 ka (Figures 20 and 22). Lake water budget modeling results, which also provide limits on temperature-precipitation combinations for 18-17 ka and 21-20 ka, are available from Lake Surprise (Ibarra et al. 2014) and Lake Franklin.

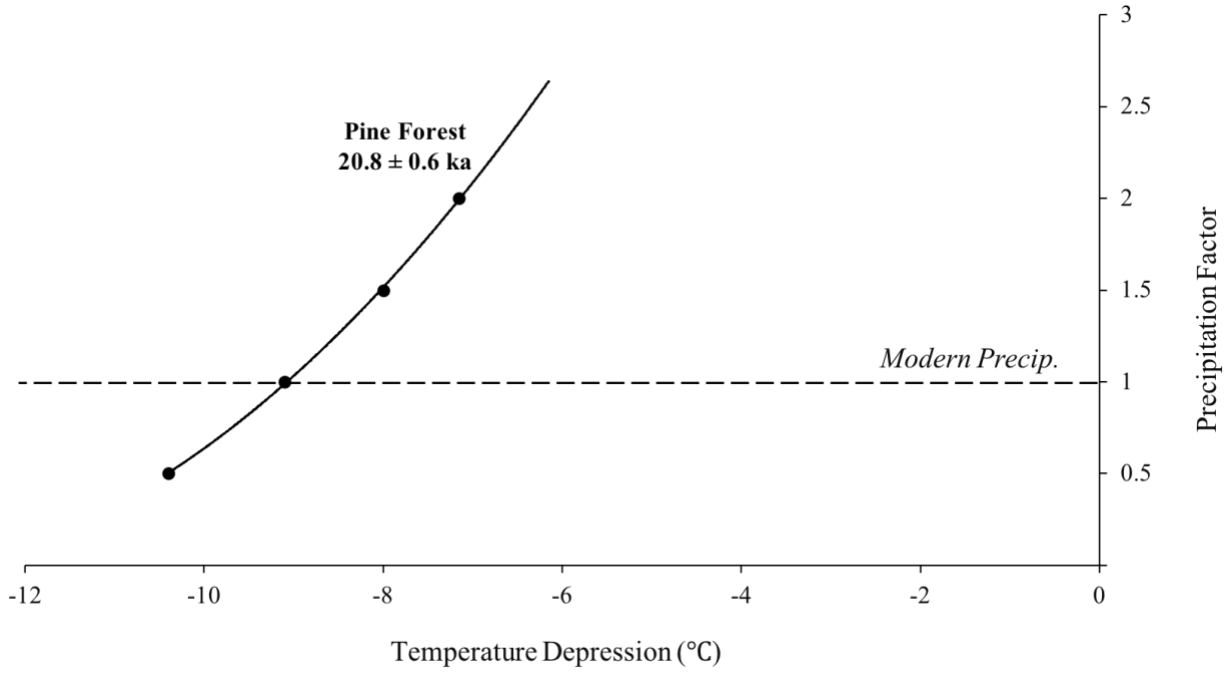

Figure 18. Combinations of precipitation changes and temperature depressions (with respect to modern) that modeled conditions necessary to sustain Pine Forest glacier stadia during the Last Glacial Maximum (21-20 ka).

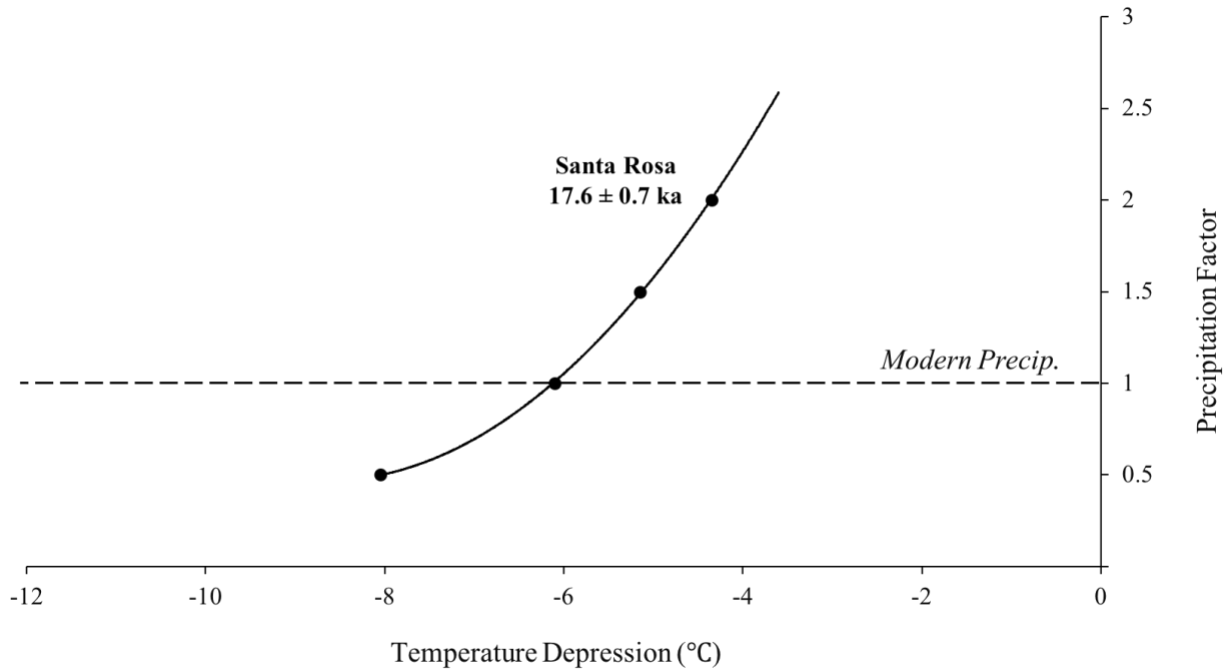

Figure 19. Combinations of precipitation changes and temperature depressions (with respect to modern) that modeled conditions necessary to sustain Santa Rosa glacier stadia during the earlier part of the Last Glacial Maximum (17-18 ka).

When comparing glacier modeling results for a given time interval in the northern Great Basin, we see that all the lines defining possible temperature-precipitation combinations plot nearly parallel to one another (Figure 20). However, comparing glacier modeling results with lake modeling results of Lake Franklin reveals intersecting trajectories of possible temperature-precipitation combinations, which yields a more unique estimate of temperature and precipitation at 18-17 ka in the northern Great Basin (Figure 21). Due to the fact that we see that the Santa Rosa glacier modeling results plot to the far right compared to the other glacier modeling results, only glacier modeling results from valleys in the Ruby and East Humboldt Mountains that are spatially close to Lake Franklin are considered.

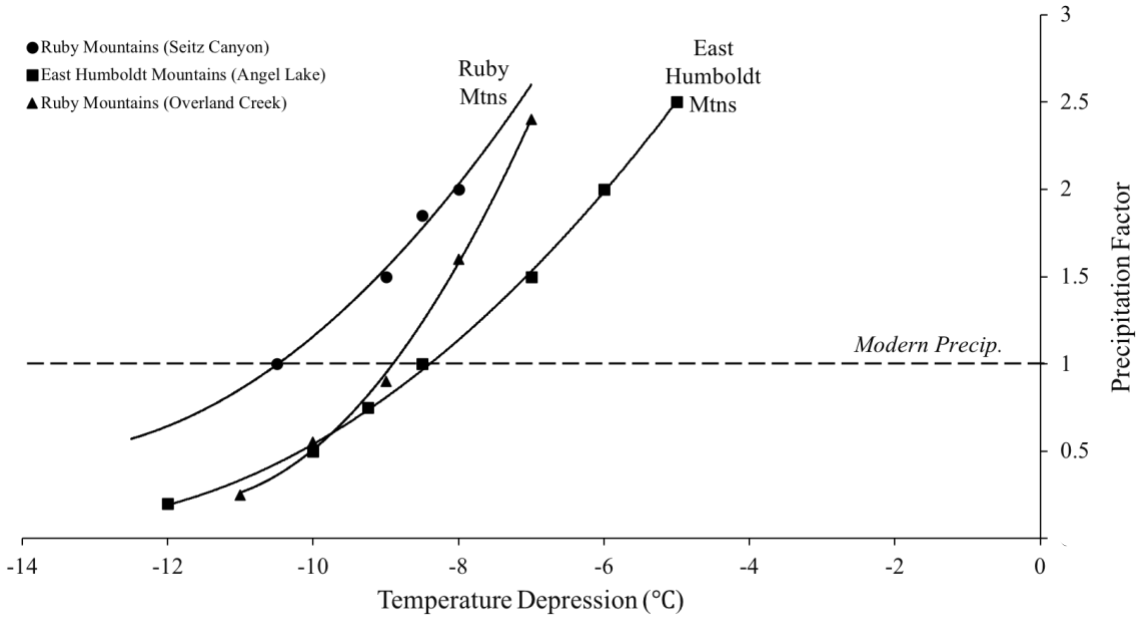

Figure 20. Combinations of precipitation changes and temperature depressions (with respect to modern) that modeled conditions necessary to sustain Ruby and East Humboldt mountains glacier stadia during the earlier interval of the Last Glacial Maximum (17-18 ka). Glacier modeling results for Seitz canyon, Overland Creek, and Angel Lake were taken from Truong et al. 2014, Reimers et al. 2018, and Bradley et al. 2015, respectively.

For this comparison, we also include the high and low *CapaS* values of inferred temperature and precipitation combinations for the modeling of Lake Franklin at a highstand of 1850 m. For glacier and lake maxima at 18-17 ka, modeling results suggest temperature depressions from -7 to -10° C and precipitation change from 1 to 1.7 × modern (Figure 21). These results indicate a colder and wetter-than-modern climate. Importantly, the combined results indicate greater-than-modern precipitation during the interval 18-17 ka, the time when most lakes of the northcentral Great Basin expanded (Munroe and Laabs, 2013) and the early part of Heinrich Stadial 1 (Hemming, 2004).

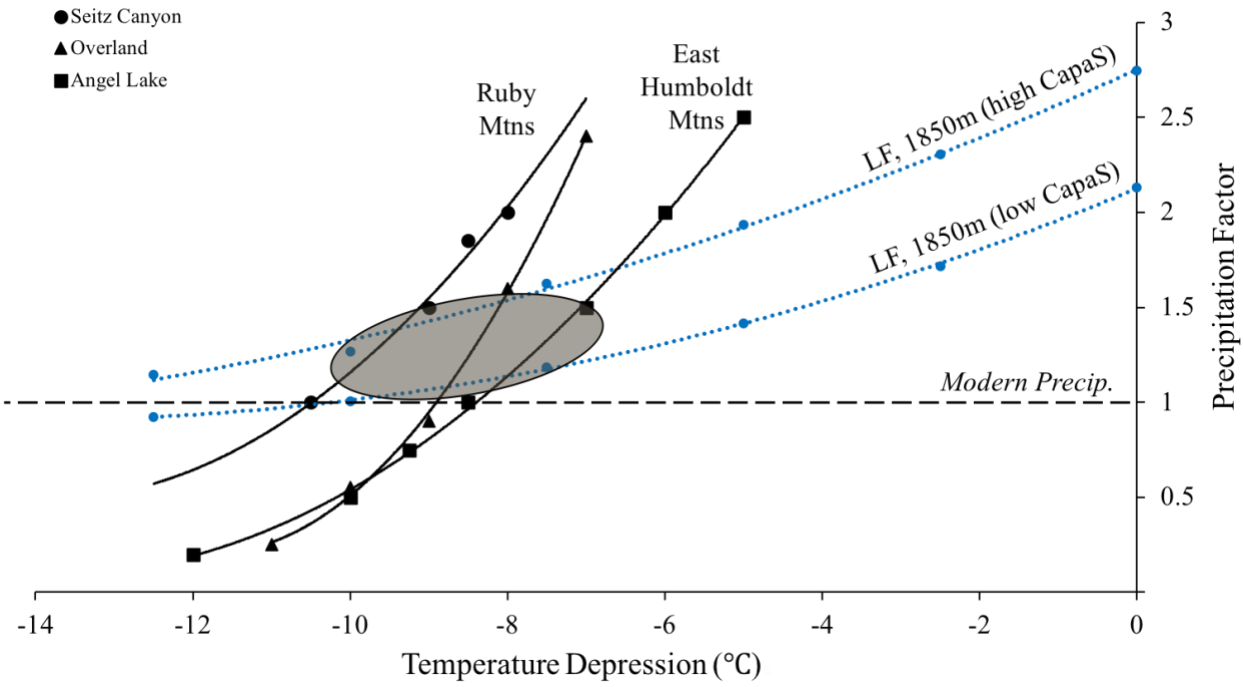

Figure 21. Combinations of precipitation changes and temperature depressions (with respect to modern) that modeled conditions necessary to sustain Ruby and East Humboldt mountains glacier stadia and Lake Franklin during the earlier interval of the Last Glacial Maximum (17-18 ka). Glacier modeling results for Seitz canyon, Overland Creek, and Angel Lake were are from Truong et al. 2014, Reimers et al. 2018, and Bradley et al. 2015, respectively.

When comparing glacier modeling results for the 21-20 ka time interval, including Seitz Canyon and Overland Creek, we see that all the lines defining possible temperature-precipitation combinations plot nearly parallel to one another (Figure 22). This suggests, as did the model results for 18-17 ka, that glacier modeling results alone do not provide a unique temperature-precipitation combination for 21-20 ka. However, comparing glacier modeling results with lake modeling results of Lake Franklin reveals intersecting trajectories of possible temperature-precipitation combinations, which yields a more unique estimate of temperature and precipitation at 21-20 ka in the northcentral Great Basin (Figure 23).

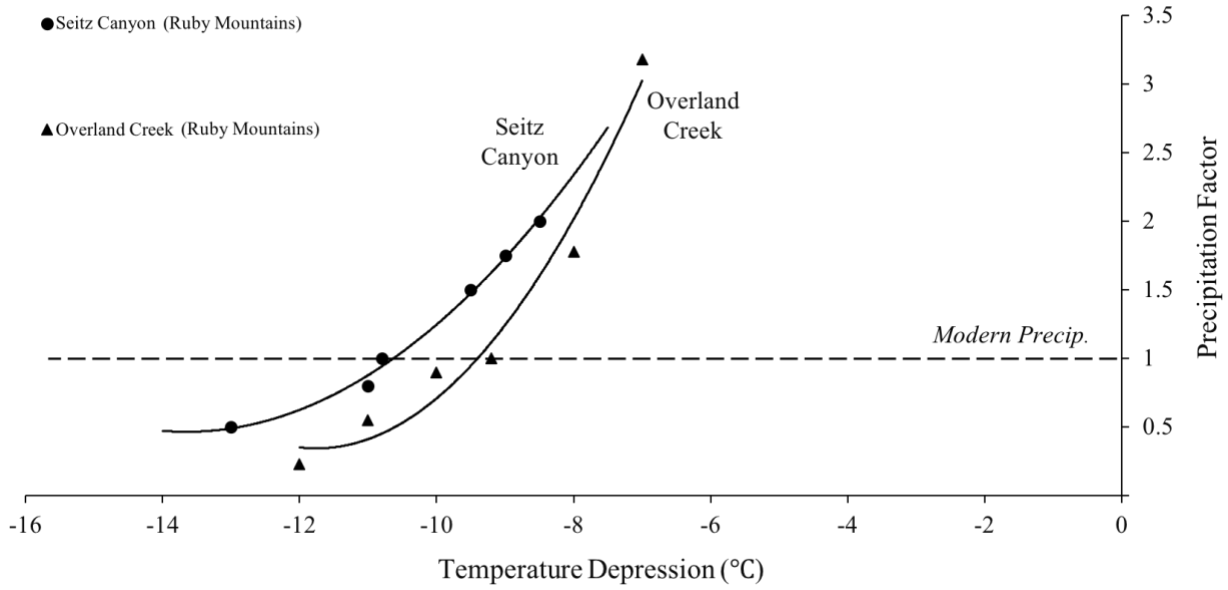

Figure 22. Combinations of precipitation changes and temperature depressions (with respect to modern) that modeled conditions necessary to sustain Ruby Mountain glaciers during the Last Glacial Maximum (21-20 ka). Glacier modeling results for Seitz canyon and Overland Creek are from Truong et al. 2014 and Reimers et al. 2018, respectively.

Only glacier modeling results that are spatially close to Lake Franklin were used for comparison. For this comparison, we include results based on the high and low *CapaS* values of inferred temperature and precipitation combinations for the modeling of Lake Franklin at a highstand of 1830 m. For glacier and lake maxima at 21-20 ka, modeling results suggest temperature depressions from -8.5 to -11° C and precipitation change from 0.8 to 1.5 × modern (Figure 23). These combined results suggest a colder and near-modern precipitation during the interval 21-20 ka for the northcentral Great Basin.

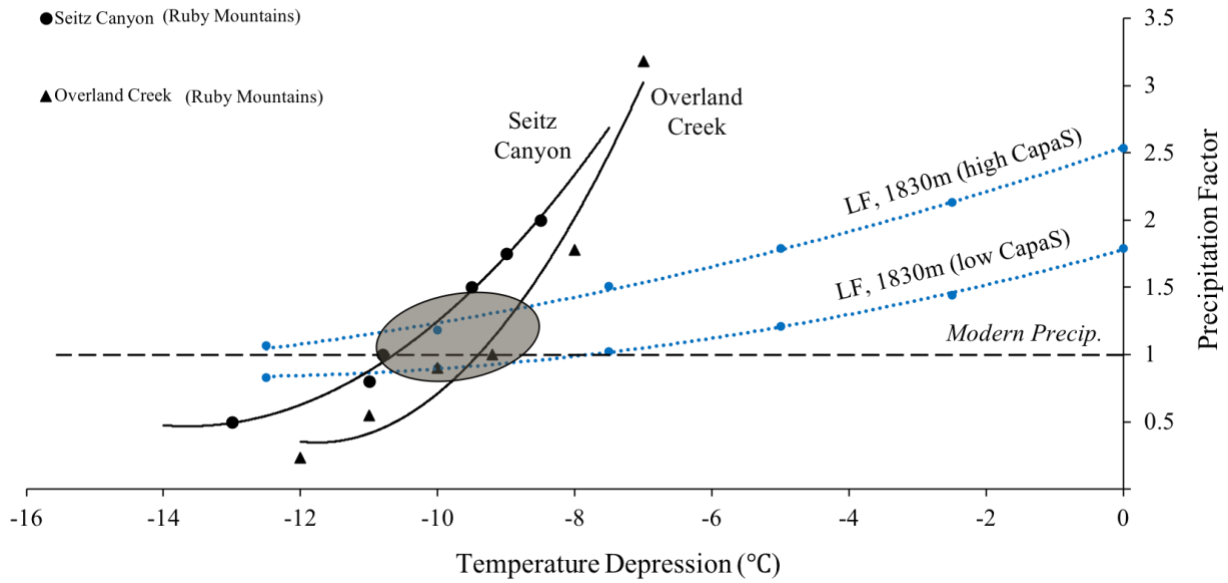

Figure 23. Combinations of precipitation changes and temperature depressions (with respect to modern) that modeled conditions necessary to sustain Ruby Mountain glacier stadia and Lake Franklin during the Last Glacial Maximum (21-20 ka). Glacier modeling results for Seitz canyon and Overland Creek are from Truong et al. 2014 and Reimers et al. 2018, respectively.

In order to identify a narrower range of possible temperature and precipitation combinations for the Pine Forest and Santa Rosa Range, glacier model output from these two locations are compared to results of a hydrologic index calculation by Ibarra et al. (2014) that produced two precipitation points for Lake Surprise, one for the interval of 21-20 ka and one for the interval of 17-18 ka. Precipitation was inferred for Lake Surprise based on an oxygen isotope mass balance model combined with an analysis of predictions from the Paleoclimate Modern Intercomparison Project 3 (PMIP3) climate model ensemble (Ibarra et al. 2014). The hydrologic index calculation, which is used at the lake highstand predicts an 85.1% increase in precipitation relative to modern. The isotope mass balance model, on the other hand predicts a 75% increase. These two percentages were used to compare against glacier modeling results at the 17-18 ka interval for the Santa Rosa Range as well as to identify a corresponding temperature and precipitation combination, specifically for the northwestern Great Basin (Figure 24).

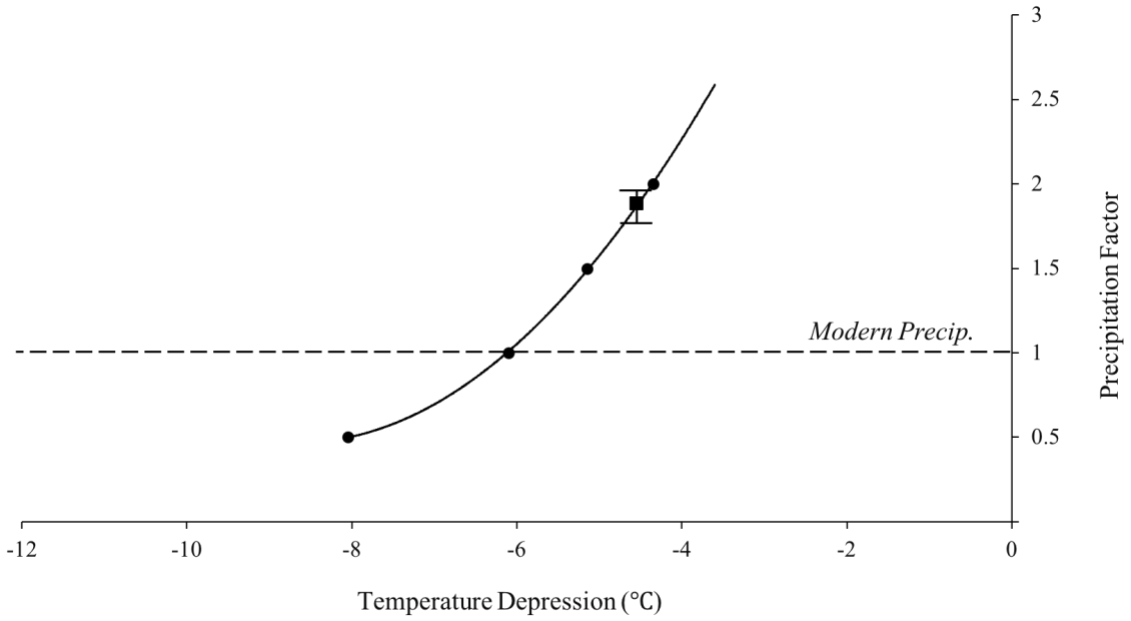

Figure 24. Combinations of precipitation changes and temperature depressions (with respect to modern) that modeled conditions necessary to sustain Santa Rosa glacier stadia during the earlier part of the Last Glacial Maximum (17-18 ka). The point represented by a black square along with a black line running through it represents a potential temperature-precipitation combination for Lake Surprise where there was a potential precipitation increase of 75-85.1%.

At the Lake Surprise highstand, the hydrologic index calculation predicted an 85.1% increase in precipitation relative to modern, greater than the isotope mass balance model, which predicted a 75% increase (Ibarra et al. 2014). By comparing these results for Lake Surprise to the Santa Rosa glacier modeling results for the interval 18-17 ka, an estimated temperature depression value of -4.5 ℃ was suggested (Figure 24), indicating a colder and wetter climate relative to modern.

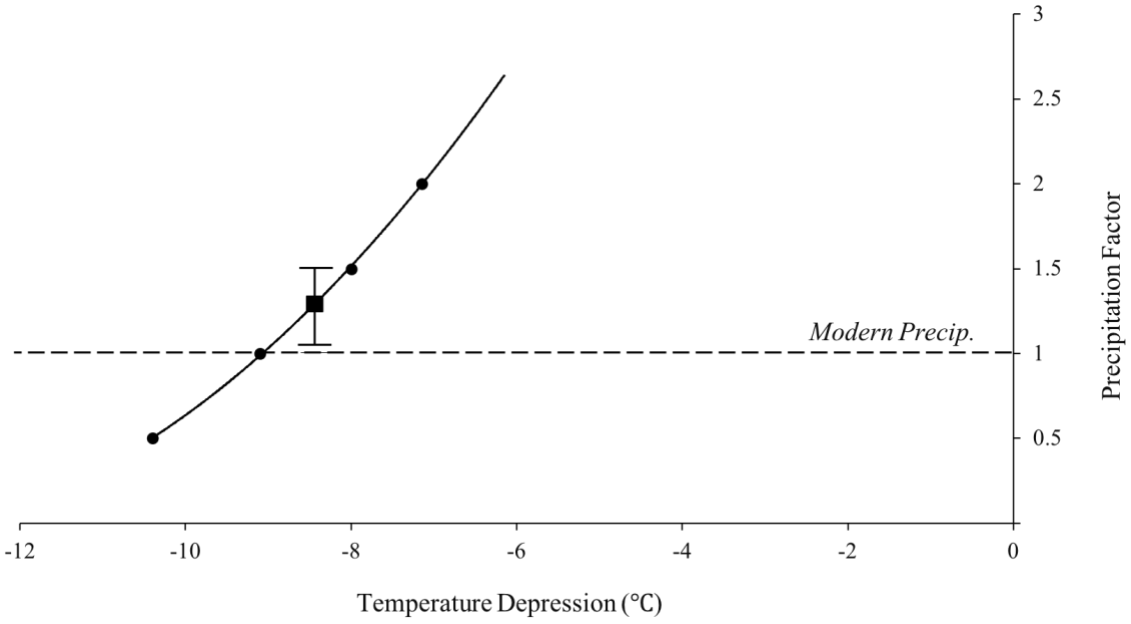

Figure 25. Combinations of precipitation changes and temperature depressions (with respect to modern) that modeled conditions necessary to sustain Pine Forest glacier stadia during the earlier part of the Last Glacial Maximum (20-21 ka). The point represented by a black square along with a black line running through it represents a potential temperature-precipitation combination for Lake Surprise where there was a potential precipitation increase of 10-53%.

At the Last Glacial Maximum, the hydrologic index predicted a 53% increase in precipitation compared to a 10% increase predicted by the isotope mass balance (Ibarra et al, 2014). By comparing these Lake Surprise modeling results to the Pine Forest glacier modeling results, an estimated temperature depression value of -8.3 ℃ was suggested (Figure 25), indicating a colder and slightly wetter climate relative to modern. Results of the northwest Great Basin and northcentral Great Basin can be compared to other areas, not just in the Great Basin, but across the western United States.

Glacier and Lake Modeling Discussion

Quirk et al. (2018) compared the chronologies of Lake Manly highstands (Death Valley, California) and glacier maxima in the Wasatch Mountains during the LGM. Results suggested temperature depression ranging from -10 to -8 ℃ and corresponding precipitation changes of

0.8-1.5 times modern. These results compare favorably to the Ruby Mountains and Lake Franklin results of inferred temperature-precipitation combinations at the LGM. These inferred paleoclimates for the northeast and northcentral Great Basin also compare favorably to model results for the northwest Great Basin. The northwest Great basin glacier modeling results for the Pine Forest Range compared to results of Ibarra et al. (2014) suggest a single temperature depression value of -8.3 ℃ and a corresponding precipitation change of approximately 1.2 times modern during the LGM. During this time, glaciers in the Pine Forest Range were at their maximum extents, but Lake Surprise was below its highstand. A colder and near-modern precipitation would have been needed to sustain glaciers at their maximum extents, while a near-modern precipitation would have sufficed for lakes below their highstand levels. We can also look at results from Oster et al. (2015) for a more regional perspective on LGM paleoclimate.

Oster et al. (2015) conducted an analysis of modeling results and proxy data, which reveal a precipitation dipole during the Last Glacial Maximum. The precipitation dipole is characterized by wetter than modern conditions in the southwestern U.S. and drier conditions in the northwest near the southern margin of the Cordilleran and Laurentide Ice Sheets, with a northwest-southeast trending transition zone across the northern Great Basin (Oster et al. 2015). The precipitation dipole model is consistent with temperature-precipitation combinations in the Pine Forest Range. Due to the precipitation dipole affect, Oster et al. (2015) concluded that a stronger jet stream and associated winter storm track was squeezed and steered across the continent by high-pressure systems best explains the regional hydroclimate patterns of the Last Glacial Maximum.

Quirk et al. (2018) also compared the chronologies of Jakes Lake (16.8-17.1 ka; Barth et al. 2016) to Wasatch glacier modeling results for the interval 15.5 ± 0.8 ka. These results

revealed a well-defined intersection at approximately -5.0 ℃ and 2 × modern precipitation (Quirk et al. 2018). These results depart slightly from the climate inferred for the Ruby and East Humboldt Mountains with Lake Franklin where there was a temperature depression of -10 to -7 ℃ and corresponding precipitation changes of 1-1.7 times modern for the 18-17 ka time interval. However, it is worth noting that Jakes Lake and the Wasatch Mountains are separated by a greater distance (>500 km) compared to the neighboring Ruby and East Humboldt Mountains and Lake Franklin, which may impact how the glacier modeling results of Quirk et al. 2018 intersect with the lake modeling results from valley far to the west and at a lower latitude.

Compared to the LGM, a colder and wetter-than-modern 18-17 ka interval is consistent with other records from the Great Basin and western North America. Munroe and Laabs (2013) identified a broad temporal correspondence between multiple pluvial lake highstands in the Great Basin and Heinrich Event 1, which they attribute to an increase in effective moisture. More specifically, they suggest that the polar jet stream migrated northward during the late LGM and early part of the last deglaciation, which primed lakes in the northern Great Basin to obtain maximum levels from subsequent increased westerly moisture delivery (Quirk et al. 2018). The increased westerly moisture delivery is attributed to the result of H1 strengthening of the Aleutian low-pressure zone and attendant strengthening of northwesterly airflow across the western United States. The northwest Great Basin glacier modeling results for the Santa Rosa Range compared to results of Ibarra et al. (2014) suggest similar precipitation changes as the northeast and northcentral Great Basin and a similar single temperature depression value of -4.5 ℃ compared to results in the northeast Great Basin by Quirk et al. (2018). Additionally, Ibarra et al. (2014) suggests a precipitation increase of 75% relative to modern during this period of H1.

Not only can we look at results from the Great Basin, but we can also compare results to other neighboring regions in the western United States.

In the areas of the Wind River Range, Wyoming, modern conditions are closer to glacial conditions than those in other ranges in the Central and Southern Rocky Mountains (Leonard et al. 2017). As a result, a smaller magnitude of climate change (temperature depression and/or precipitation enhancement) would be required for large-scale glaciation in that range compared to elsewhere in the region (Leonard et al. 2017). Other ranges in Wyoming and Colorado require more climate change in order for large-scale glaciation to begin, and major glaciated ranges in Utah, including the Wasatch Range, require still a greater magnitude of climate change for glaciation to initiate (Leonard et al. 2017). This difference can also be compared to results in the Pine Forest Range at the LGM where similar to the Wasatch Range, a greater magnitude of climate change would be required in order to initiate glaciation compared to ranges in Wyoming and Colorado. For the Wasatch Range, this difference could reflect LGM precipitation enhancement, possibly derived from the surface of Lake Bonneville immediately upwind of this range (Leonard et al. 2017). For the Pine Forest Range, this difference could also reflect LGM precipitation enhancement, although these mountains lack a proximal source of precipitation other than the relatively small Lake Surprise.

CHAPTER 5: CONCLUSION

This thesis presents 17 new cosmogenic exposure ages from the Santa Rosa and Pine Forest Ranges in the northwestern Great Basin, Nevada. These ages were calculated using newer production rate models (Borchers et al. 2016; Lifton et al., 2015) and the Lifton-Sato-Dunai scaling model (Lifton et al., 2014; Shakun et al. 2015), and were then used to establish the late Pleistocene glacial chronology of the two ranges. The cosmogenic chronology of a terminal moraine in the Pine Forest Range coincides with the latter part of the LGM. A single exposure age on a younger moraine upvalley of the terminal moraine represents the time of a later advance or pause in ice retreat, although additional cosmogenic exposure ages are needed to obtain an accurate numeric age of this moraine. The cosmogenic exposure age of a terminal moraine in the Santa Rosa Range, on the other hand, coincides well with the 18-17 ka interval. Younger moraines upvalley shows an average age of 16.1 ± 0.6 ka, which suggests that ice readvanced to, or persisted within, 90% of its maximum length after the terminal moraine was abandoned ca. 18.3 ± 0.9 ka, likely in step with the late highstand of nearby Lake Surprise at 16-15 ka. Developing chronologies of moraines in the Santa Rosa and Pine Forest Ranges has helped to precisely limit the relative timing of glacier and lake maxima.

Utilizing the differing sensitivities of pluvial lakes and late Pleistocene glaciers to temperature and precipitation, we have combined numerical models of coeval glaciers and lakes in the northcentral Great Basin as well as glaciers and one lake in the northwestern Great Basin to limit the range of possible late Pleistocene climates. The LGM featured a precipitation dipole effect (Oster et al. 2015). The precipitation dipole suggests wetter than modern conditions in the southwestern United States, drier conditions in the Pacific Northwest through the Rockies, as well as a northwest-southeast transition zone from wetter to drier conditions across the northern

Great Basin during the LGM (Oster et al. 2015). The northwest-southeast transition zone from wetter to drier conditions across the northern Great Basin can be compared to results from the Pine Forest Range and Lake Surprise in the northwest to results from Lake Franklin and glacier modeling results (Ruby Mountains) in the northcentral Great Basin. Ibarra et al. (2014) suggests a precipitation increase of 53% relative to modern for Lake Surprise during this period. From this, an estimated temperature depression of -8.3 ℃ is suggested based on glacier modeling results reported here. These results indicate wetter and colder climate conditions for the northwest Great Basin. As we move along the northern Great Basin transition zone to the northcentral Great Basin, model results reported here suggest a precipitation increase of again up to 50% and temperature depressions ranging from -11 to -8.5 ℃, indicating both wetter and colder climate conditions for the northcentral Great Basin. However, modeling results suggest a range of precipitation change from 0.8 to 1.5 × modern, indicating that near-modern precipitation or possibly drier climate conditions were also possible for the northcentral Great Basin. Overall, the LGM featured a climate more favorable for glacier maxima compared to lake highstands.

The interval 18-17 ka, corresponding to the early part of Heinrich Stadial 1, featured the expansion of many pluvial lakes in the northern Great Basin. Glaciers in the Wasatch Mountains, Ruby Mountains, and East Humboldt Mountains were at or near their maximum extent during this time. This suggests a climate favorable for both glaciers and lakes, potentially wetter than the preceding interval of the LGM. Glacier modeling results from the northcentral Great Basin (Ruby and East Humboldt Mountains) compared to Lake Franklin modeling results suggest a precipitation increase of up to 50-75% and temperature depressions ranging from -7 to -10 ℃, indicating wetter and colder climate conditions for the northcentral Great Basin. Results from the Santa Rosa Range glacier modeling and hydrologic modeling of Lake Surprise (Ibarra et al.

2014) suggest a precipitation increase of 75-85% compared to modern. From this, an estimated temperature depression of -4.5 ℃ is inferred, indicating a smaller temperature depression and wetter climate conditions compared to the northcentral Great Basin. Previous inferences of enhanced delivery of moisture from the Pacific Ocean during Heinrich Stadial 1 to parts in the northwestern Great Basin is consistent with model results reported here indicating both wetter and colder-than-modern climate at 18-17 ka.

Our work from the Santa Rosa and Pine Forest Ranges affirms the hypothesis that the LGM was regionally characterized as cold and dry relative to a warmer and wetter climate during the subsequent interval 18-17 ka. Compared to the northcentral and northeast Great Basin, however, our ability to narrow the range of possible LGM and subsequent deglacial paleoclimate is limited for the northwest Great Basin. This is due to the limited number of pluvial lakes in the area to which glacier modeling results can be compared and the relatively late highstands of pluvial lakes Lahontan, Surprise, and Chewaucan compared to intervals of moraine deposition. Future work should include additional cosmogenic exposure dating of moraines across the northwest Great Basin, chiefly recessional moraines that may overlap in time with pluvial lake highstands. Further development of other paleoclimate proxies may also help to link climate in the northwestern Great Basin to other glaciated regions across the Great Basin and the western United States.

REFERENCES

Balco, G., Stone, J., Lifton, N., and Dunai, T., 2008, A complete and easily accessible means of calculating surface exposure ages or erosion rates from ^{10}Be and ^{26}Al measurements: Quaternary Geochronology, v. 3, p. 174-195.

Balco, G., 2011, Contributions and unrealized potential contributions of cosmogenic-nuclide exposure dating to glacier chronology, 1990-2010: Quaternary Science Reviews, doi: 10.1016/j.quascirev.2010.11003.

Barth, C., Boyle, D.P., Hatchett, B.J., Bassett, S.D., Garner, C.B., and Adams, K.D., 2016, Late Pleistocene climate inferences from a water balance model of Jakes Valley, Nevada (USA): Journal of Paleolimnology, v. 56, p. 109–122.

Bennett, M.R., and Glasser, N.F., 2009, Glacial Geology: Ice Sheets and Landforms; Textbook published by Wiley-Blackwell, p. 1-20.

Benson, L.V., Lund, S.P., Smoot, J.P., Rhode, D.E., Spencer, R.J., Verosub, K.L., Louderback, L.A., Johnson, C.A., Rye, R.O., and Negrini, R.M., 2011, The rise and fall of Bonneville between 45 and 10.5 ka: Quaternary International, v. 235, p. 57-69, doi:10.1016/j.quaint.2010.12.2014.

Birkel, S.D., Putnam, A.E., Denton, G.H., Koons, P.O., Fastook, J.L., Putnam, D.E., and Maasch, K.A., 2012, Climate inferences from a glaciological reconstruction of the late Pleistocene Wind River ice cap, Wind River Range, Wyoming: Arctic, Antarctica, and Alpine Research, v. 44, p. 265-276.

Borchers, B., Marrero, S., Balco, G., Caffee, M., Goethring, B., Lifton, N., Nishiizumi, K., Phillips, F., Schaefer, J., and Stone, J., 2016, Geological calibration of spallation

production rates in the CRONUS-Earth project: Quaternary Geochronology, v. 31, p. 188-198.

Bradley, R.A.A., and Laabs, B.J.C., 2015, Climate change during the last Pleistocene glaciation in northern Nevada inferred from numerical glacial modeling, Angel Lake type locality, East Humboldt Range, Nevada, U.S.A: Geological Society of America, Abstracts with Programs, v. 47, no. 3, p. 114.

Clark, P.U., Dyke, A.S., Shakun, J.D., Carlson, A.E., Clark, J., Wohlfarth, B., Mitrovica, J.X., Hostetler, S.W., and McCabe, A.M., 2009, The Last Glacial Maximum: Science, vol. 325, p. 710-711.

Condom, T., Coudrain, A., Dezetter, Alain., Brunstein, D., Delclaux, F., and Jean-Emmanuel, S., 2004, Transient Modelling of lacustrine regressions: two case studies from the Andean Altiplano: Hydrological Processes, v. 18, p. 2395-2408.

Daly, C., Halbleib, M., Smith, J.I., Gibson, W.P., Doggett, M.K., Taylor, G.H., Curtis, J., and Pasteris, P.P., 2007, Physiographically sensitive mapping of climatological temperature and precipitation across the conterminous United States: International Journal of Climatology, doi: 10.1002/joc.1688, p. abstract.

Ferragut, G., Laabs, B.J.C., Amidon, W.A., and Munroe, J.S., 2017, Constraining Late Pleistocene climate of the northeastern Great Basin using mass balance modeling of paleolakes and glaciers: Geological Society of America, Abstracts with Programs, v. 49, no. 6, p. 361-3, doi: 10.1130/abs/2017AM-306260.

Griffin, D., Anchukaitis, K.J., 2014, How unusual is the 2012-2014 California drought: Geophysical Research Letters, v. 41, issue 24, p. 9017-9023.

Harrison, S., Rowan, A.V., Glasser, N.F., Knight, J., Plummer, M.A., and Mills, S.C., 2014, Little Ice Age glaciers in Britain: Glacier–climate modelling in the Cairngorm Mountains: The Holocene, v. 24, p. 135– 140.

Hemming, S.R., 2004, Heinrich events; massive late Pleistocene detritus layers of the North Atlantic and their global climate imprint: Reviews of Geophysics, v. 42, RG 1005.

Heisinger, B., Lal, D., Jull, A.J.T., Kubik, P., Ivy-Ochs, S., Knie, K., and Nolte, E., 2002a, Production of selected cosmogenic radionuclides by muons: 2. Capture of negative muons. Earth and Planetary Science Letters 200 (3-4), 357-369.

Heisinger, B., Lal, D., Jull, A.J.T., Kubik, P., Ivy-Ochs, S., Neumaier, S., Knie, K., Lazarev, V., and Nolte, E, 2002b, Production of selected cosmogenic radionuclides by muons 1. Fast muons. Earth and Planetary Science Letters 200 (3-4), 345-355.

Hudson, A.M., Quade, J., Guleed, A., Boyle, D., Bassett, S., Huntington K.W., De Los Santos, M.G., Cohen, A.S., Xiangfeng Wang, and Ke Lin., 2017, Stable C, O and clumped isotope systematics and 14C geochronology of carbonates from the Quaternary closed-basin lake system, Great Basin, USA: Implications for paleoenvironmental reconstructions using carbonates: ScienceDirect, v. 212, p. 274-302.

Ibarra, D.E., Egger, A.E., Weaver, K.L., Harris, C.R., and Maher, K., 2014, Rise and fall of late Pleistocene pluvial lakes in response to reduced evaporation and precipitation: Evidence from Lake Surprise, California: Geological Society of America Bulletin, v. 126, no. 11-12, p. 1-29.

Laabs, B.J.C., and Munroe, J.S., 2016, Late Pleistocene mountain glaciation in the Lake Bonneville Basin, *in* Oviatt, C.G., and Schroeder, J., editors, Lake Bonneville: A Scientific Update: Elsevier, Amsterdam, p. 462-503.

Laabs, B.J., Munroe, J.S., Best, L.C., and Caffee, M.W., 2013, Timing of the last glaciation and subsequent deglaciation in the Ruby Mountains, Great Basin, USA: Earth and Planetary Science Letters, v. 361, p.16-25.

Laabs, B.J.C., Marchetti, D.W., and Munroe J.S., 2011, Chronology of latest Pleistocene mountain glaciation in the western Wasatch Mountains, Utah, U.S.A: Quaternary Research 76: 272-284.

Lachniet, M.S., Denniston, R.F., Asmerom, Y., and Polyak, V.J., 2014, Orbital control of western North America atomospheric circulation and climate over two glacial cycles: Nature Communications, v.5, p. 1-8.

Leonard, E.M., Laabs, B.J., Plummer, M.A., Kroner, R.K., Brugger, K.A., Spiess, V.M., Refsnider, K.A., Xia, Y., and Caffee, M.W., 2017, Late Pleistocene glaciation and deglaciation in the Crestone Peaks area, Colorado Sangre de Cristo Mountains, USA—chronology and paleoclimate: Quaternary Science Reviews, v. 158, p. 127–144.

Lifton, N., Sato, T., and Dunai, T.J., 2014, Scaling in situ cosmogenic nuclide production rates using analytical approximations to atmospheric cosmic-ray fluxes: Earth and Planetary Science Letters, v. 386, p.149-160.

Lifton, N., Caffee, M., Finkel, R., Marrero, S., Nishiizumi, K., Phillips, F.M., Goethring, B., Gosse, J., Stone, J., Shaefer, J., and Theriault, B., 2015, In situ cosmogenic nuclide production rate calibration for the CRONUS-Earth project from Lake Bonneville, Utah, shoreline features: Quaternary Geochronology, v. 26, p. 56-69.

Lyle, M. et al. 2012, Out of the tropics: The Pacific, Great Basin Lakes, and Late Pleistocene water cycle in the western United States. Science 337, 1629_1633.

Munroe, J.S., Laabs, B.J.C., Oviatt, C.G., and Jewell, P.W., 2015. New investigations of Pleistocene pluvial and glacial records from the northeastern Great Basin, in Rosen, M.R. (ed.), Sixth International Limnogeology Congress – Field Trip Guidebook, Reno, Nevada: U.S. Geological Survey Open-File Report 2015-1108, 1-30.

Munroe, J.S., and Laabs, B.J., 2013, Temporal correspondence between pluvial lake highstands in the southwestern US and Heinrich Event 1: Journal of Quaternary Science, v. 28, no. 1, p.49-58.

Munroe, J.S., and Laabs, B.J., 2013, Latest Pleistocene history of pluvial Lake Franklin, northeastern Nevada, USA: GSA Bulletin, v. 125, no. ¾, p. 322-323.

Osborn, G., and Bevis, K., 2001, Glaciation in the Great Basin of the western United States: Quaternary Science Reviews, v. 20, p. 1377–1410.

Oster, J.L., Ibarra, D.E., Winnick, M.J., and Maher, K., 2015, Steering of westerly storms over western North America at the Last Glacial Maximum: Nature Geoscience, v. 8, p.201, doi: 10.1038/NGEO2365.

Oster, J.L., and Kelley N.P., 2016, Tracking regional and global teleconnections recorded by western North American speleothem records: Quaternary Science, v. 149, p. 18-33.

Owen L.A., Finkel R.C., and Minnich R.A., 2003, Extreme southwestern margin of late Quaternary glaciation in North America: timing and controls: Geology 31: 729-732.

Phillips, F.M., and Zreda M, Plummer M.A., 2009, Glacial geology and chronology of Bishop Creek and vicinity, eastern Sierra Nevada, California: Geological Society of America Bulletin 121: 1013-1033.

Phillips, F.M, 2016, Cosmogenic nuclide data sets from the Sierra Nevada, California, for assessment of nuclide production models: 1. Late Pleistocene glacial chronology: Quaternary Geochronology, v. 35, p. 119-129.

Phillips, F.M, 2017, Glacial Chronology of the Sierra Nevada, California, from the Last Glacial Maximum to the Holocene: Cuadernos de Investigacion Geografica, v. 43, no. 2, pp. 527-552.

Pierce, K.L., 2003, Pleistocene glaciations of the Rocky Mountains: Developments in Quaternary Sciences, v. 1, p.63-76.

Plummer, M.A., and Phillips, F.M., 2003, A 2-D numerical model of snow/ice energy balance and ice ow for paleoclimatic interpretation of glacial geomorphic features: Quaternary Science Review, v. 22, p. 1389-1406.

Prudic, D.D., Niswonger, R.G., and Plume, R.W., 2005, Trends in streamflow on the Humboldt river between Elko and Imlay, Nevada, 1950-1999: Scientific Investigations Report, 2005-5199.

Quirk, B.J., Moore, J.R., Laabs, B.J.C., Caffee, M.W., and Plummer, M.A., 2018, Termination 11, Last Glacial Maximum, and Lateglacial chronologies and paleoclimate from Big Cottonwood Canyon, Wasatch Mountains, Utah: GSA Bulletin, doi.org/1130/B31967.1, p. 1-14.

Reheis, M.C., 1999, Extent of Pleistocene lakes in the western Great Basin: U.S. Geological Survey Miscellaneous Field Studies Map 2323, https://doi.org/10.3133/mf2323.

Reimers, A.C., and Laabs, B.J.C., 2016, Mountain glacier retreat rates during the last Pleistocene glaciation in the western United States. Geological Society of America, Abstracts with Programs, v. 48, no. 7, p. 81-8.

Rowan, A.V., Brocklehurst, S.H., Schultz, D.M., Plummer, M.A., Anderson, L.S., and Glasser, N.F., 2014, Late Quaternary glacier sensitivity to temperature and precipitation distribution in the Southern Alps of New Zealand: Journal of Geophysical Research., Earth Surface, v. 119, p. 1064–1081.

Russell, I.C., 1885, Geological History of Lake Lahontan, a Quaternary Lake of Northwestern Nevada: U.S. Geological Survey Report M-0011, p.288.

Shakun, J.D., Clark, P.U., He, F., Lifton, N.A., Zhengyu, L., and Otto-Bliesner, B.L., 2015, Regional and global forcing of glacier retreat during the last glaciation: Nature Communications 6, Article number: 8059, p. 4-5.

Sharp, R.P., 1938, Pleistocene glaciation in the Ruby-East Humboldt Range, northeastern Nevada, with abstract in German by Kurt E. Lowenstein: Journal of Geomorphology, v. 1, p. 296-323.

Simpson, J.H., 1876, Report of Explorations across the Great Basin of the Territory of Utah in 1859: Washington, D.C., Publisher unknown.

Smith, J.G., 1973. Geologic map of the Duffer Peak Quadrangle, Humboldt county, Nevada. U.S. Geological Survey, Miscellaneous Geologic Investigations Map I-606, Scale 1:48,000.

Steen, D., and Laabs, B.J., 2015, Water balance modeling and paleoclimate investigation of Pleistocene pluvial Lake Clover, Nevada, USA: Undergraduate Thesis for the department of geological sciences at SUNY Geneseo, p. 16-19.

Stewart, J.H., 1980, Geology of Nevada. Nevada Bureau of Mines and Geology Special Publication 4, 136 p.

Thompson, R.S., 1992, Late Quaternary environments in Ruby Valley, Nevada: Quaternary Research, v. 37, p.1-15.

Truong, K.T., Laabs, B.J.C., and Lam, J.J., 2014, Climate change during the last glaciation in the northern Great Basin inferred from numerical modeling of glaciers in the Ruby Mountains, northern Nevada. Geological Society of America, Abstracts with Programs, v. 46, no. 6, p. 557.

Vikre, P.G., 1985, Geologic map of the Buckskin Mountain Quadrangle, Nevada. Nevada Bureau of Mines and Geology Map 88, scale 1: 24,000.

Walker, J.D., Geissman, J.W., Bowring, S.A., and Babcock, L.E., compilers., 2018, Geologic Time Scale v. 5.0: Geological Society of America, doi.org/10.1130/2018.CTS005R3C.

Worona, M.A., and Whitlock C., 1995, Late Quaternary vegetation and climate history near Little Lake, central Coast Range, Oregon. Geological Society of America Bulletin, v. 107, no. 7, p. 867-876.

APPENDIX A: METHODS

Field Methods

Moraine boulders collected throughout the Santa Rosa and Pine Forest Ranges were targeted for cosmogenic ^{10}Be surface exposure dating. Quartz-bearing boulders, including granites and quartzites that were deposited on moraine crests were primary targets. For both localities (Santa Rosa and Pine Forest), samples were collected using a portable rock saw, sledge-hammer, and chisel. Sample thicknesses ranged from 2-8 cm while sample heights ranged from 50- 180 cm respectively. The number of samples collected from both field sites were based on the type of moraine and the availability of suitable targets. GPS data, including latitude and longitude, and elevation were collected as well as topographic shielding data. Topographic shielding refers to the proportion of the incoming cosmic radiation that is shielded by the surrounding topography, including valley walls, mountain peaks, etc. The scaling factor can be defined as the ration of the unshielded (total minus shielded) to the total cosmic ray flux. Topographic Shielding data were collected in the field by measuring valley walls, mountain peaks, etc. as the angle above the horizon at 10 degree increments around the full 360-degree view. GPS and topographic shielding data were also collected in order to estimate an approximate production rate for each sample that was collected.

Additionally, in order to identify the extents of glaciers in the valleys that have been sampled for cosmogenic ^{10}Be exposure dating, field mapping was conducted by Dr. Benjamin Laabs and Dr. Jeff Munroe. The mapped extents for both the Santa Rosa and Pine Forest Ranges were mapped using topographic maps and aerial images as well as the use of a GPS. Additional mapping information for these two ranges is needed in the future and will give whomever the

chance to model glaciers in multiple valleys, which would help to improve the estimates of temperature and precipitation during the last glaciation.

Lab Methods

All of the samples collected from the two field sites were prepared in the cosmogenic ^{10}Be surface exposure dating lab located at NDSU using methods modified from Laabs et al. (2013) and Liccardi (2017). Samples were first crushed, milled, and sieved to a desired grain size of approximately 250-500 microns. Fragments of the milled samples that are coarser than about 500 microns are generally polyminerallic, and fragments smaller than about 250 microns are too fine to survive chemical treatment. Therefore, the grain size of interest is between these two cutoff values and is captured in a sieve. In order to get to pure quartz, samples were then brought through a series of steps that would isolate the quartz grains from any impurities. For the granite samples, a hand magnet and froth flotation were used to isolate quartz grains. Each granite sample that was collected, was first laid out onto a piece of parchment paper. Then, a hand magnet wrapped in a kimwipe would be moved over the sample, continuously, until the kimwipe came up clear, which tells us that the sample is free of magnetized grains. After all the samples were de-magnetized, the samples were then taken through froth flotation. Separation of quartz grains from other felsic minerals in samples of crushed rock or sediment can be a challenge due to similar densities and chemical properties. However, froth flotation can be used to separate quartz grains from other felsic minerals, including, feldspars. Froth flotation physically separates grains of crushed rock based on differences in the tendency of air bubbles to adhere to surfaces of felsic minerals (Whelan and Brown, 1956). Samples are first pre-treated in dilute hydrofluoric acid (HF) for one hour. This pretreatment renders feldspar and muscovite surfaces hydrophobic, while quartz surfaces remain hydrophilic. Therefore, in a carbonated solution with the addition

of 3-4 drops of tea tree oil, hydrophobic grains adhere to the bubbles and float whereas hydrophilic grains (quartz) sink and stay at the bottom. Froth flotation was used specifically to maximize the degree of mineral separation and the recovery of quartz grains so that there are less complications to arise in the following steps.

Following de-magnetization and froth flotation, the quartz purification process was accomplished by repeated etching in dilute hydrochloric and hydrofluoric and nitric acids. Samples were etched in hydrochloric acid for 4-6 hours until the solution reached clarity and stopped changing color (approximately 4-5 times). Hydrochloric acid etching was used in order to remove organic material and for breaking up some (but not all) lingering mafic minerals from the samples. Dilute hydrofluoric acid (HF) and nitric acid (HNO_3) were then used to dissolve remaining feldspars as well as the removal of metoric beryllium from quartz grain surfaces. Repeated etching in hydrofluoric and nitric acids ranging from 0.5% to 3% depending on the mass of the sample was used. After repeated etching (4-8 times), quartz purity tests were performed on the samples. A quartz purity solution comprised of hydrofluoric and sulfuric acid was used on the samples. If the samples did not pass the quartz purity test, the sample would be etched in hydrofluoric and nitric acids again, and would then be re-tested. In addition to the quartz purity tests, samples were also looked at under a microscope to determine whether they are pure.

A series of chemistry steps, including aliquot dissolution and ICP Analysis were then performed on the samples. The purified quartz fraction was first spiked with a commercially made ^{9}Be carrier solution purchased from SPEX CentriPrep. Procedural blanks were prepared using the same mass of carrier that was added to the samples. After the samples are massed and spiked with a Be carrier solution and Al carrier solution (for the blank), they are dissolved in

concentrated HF. Once the samples have been completely dissolved, the samples are then spiked with 3 mL of 6 M HCL and 1 mL of 8 M HNO_3. The samples are then set in a laminar flow box to be dried down. When the HF solutions have completely evaporated, the samples are removed and are set to the side to cool. The dried material (metal chloride and fluoride salts) range in color from white to orange-brown, to gray-green, depending on the metals present. To convert the chlorides and fluorides to chloride form, a small graduated cylinder is used to add 25 mL of trace metal grade 6 M HCL to the dried material. The samples are then added to the hotplate to dry at 235 degrees C. The continued addition and dry-down of the samples (approximately 2 times) will convert the chlorides and fluorides to chloride form. At this point in the processing, the samples will consist of Be, Al, Ca, Ti, and Fe in a 6 M HCL solution. The next procedure involves passing each sample solution through a column of organic resin to remove Fe and some Ti (anion columns). The anion columns have a greater volume of resin and are yellow in color. Before the samples are loaded, the columns are stripped and conditioned to remove any residual iron off the columns. Once the samples have been run through the anion columns, 1 mL of H_2SO_4 is added to each sample and are then dried down at 235 degrees. The metals present in the 6 M HCL solution include Be, Al, and Ti. However, some organic compounds that might have bled from the column resin are also present. They appear in the next step as a black, charry solid. The continued addition of 2% H_2O_2 and 1% H_2SO_4 and the dry-down of the samples will convert the chlorides to sulfide form. Eventually the sample should dry down to a small white cake or a viscous bead of involatile H_2SO_4. At this point in the processing, samples consist of Be, Al and Ti in a dilute H_2SO_4 solution. Similar to the anion exchange column, the next procedure involves passing each sample solution through a column of organic resin; however, in this procedure, the goal is to remove Ti and separate Be and Al. For the Titanium elution, the FEP squirt bottle is

used to measure out 6 bed volumes of 0.58 M H_2SO_4 with trace H_2O_2 and is then slowly added to the column reservoir. For the Be elution, the FEP squirt bottle is used to measure out 5.5 bed volumes of 1.2 M HCL and is then slowly added to the column reservoir. For the Al elution, the FEP squirt bottle is used to measure out 4 bed volumes of 4 M HCL and is then added to the column reservoir. The Be cuts are then placed in the laminar flow box to dry down until only a small, clear nonvolatile bead of liquid remains. After the cuts of Ti, Be and Al have been collected from the cation columns, most samples will require immediate treatment of only the Be cut. The next step involves a series of steps in order to generate $Be(OH)_2$, which is then converted to BeO for the final preparation of the AMS target. Once the samples have dried down, 8 mL of a 1% HNO_3 solution is added to each sample. Working with one sample at a time, a transfer pipette is used to add 6 drops of 30 % NH_4OH and 4 drops of 15 % NH_4OH. By drawing a minimal amount of fluid, the pH of the sample is tested. If the pH is at 8.5, then a cloudy precipitate will be visible in the test tube and the samples can then be converted from $Be(OH)_2$ to BeO. Once the samples have been transferred to low-boron quartz vials, dried, and then ignited with a blowtorch, the samples are then ready for loading. The final step is the loading of the samples into cathodes mixed with a niobium powder, in which the samples are then sent to PRIME lab at Purdue University.

APPENDIX B: TABLES FOR CHRONOLOGY

Table B1. Input data for cosmogenic ^{10}Be surface exposure age calculation.

Sample name	Latitude (DD)	Longitude (DD)	Elevation (masl)	Elv/pressure flag	Thickness (cm)	Density (g cm-3)	Shielding correction	Erosion rate (cm yr-1)	[Be-10] atoms g-1	+/- atoms g-1
SANTA ROSA RANGE										
Granite Peak terminal										
SRSA-14	41.6766	-117.5934	2609	std	5.5	2.7	0.9859	0	5.16E+05	2.16E+04
SRSA-15	41.6765	-117.5935	2614	std	5	2.7	0.9859	0	4.80E+05	1.78E+04
SRSA-16	41.6764	-117.5937	2622	std	3	2.7	0.9859	0	5.08E+05	2.16E+04
SRSA-17	41.6763	-117.5937	2627	std	5	2.7	0.9859	0	4.99E+05	1.79E+04
SRSA-18	41.6764	-117.5934	2623	std	3	2.7	0.9859	0	5.48E+05	2.66E+04
Granite Peak recessional										
SRSA-8	41.6749	-117.5922	2639	std	3.5	2.7	0.9846	0	4.60E+05	1.85E+04
SRSA-9	41.6749	-117.5921	2637	std	4.5	2.7	0.9846	0	4.63E+05	1.80E+04
SRSA-21	41.6753	-117.5931	2648	std	5	2.7	0.9859	0	4.87E+05	1.66E+04
SRSA-22	41.6753	-117.5932	2648	std	3	2.7	0.9859	0	5.03E+05	2.23E+04
SRSA-24	41.6749	-117.5931	2653	std	3	2.7	0.9859	0	4.74E+05	1.89E+04
SRSA-25	41.6749	-117.5932	2656	std	3.5	2.7	0.9859	0	4.48E+05	1.43E+04
PINE FOREST RANGE										
Duffer Peak terminal										
PF-08	41.6821	-118.7223	2441	std	4	2.7	0.9959	0	5.55E+05	1.46E+04
PF-09	41.6824	-118.7222	2441	std	4.5	2.7	0.9959	0	5.49E+05	1.43E+04
PF-10	41.6835	-118.7221	2433	std	3.5	2.7	0.9958	0	5.19E+05	1.34E+04
PF-11	41.6836	-118.7219	2439	std	5.5	2.7	0.9958	0	5.51E+05	1.55E+04
PF-12	41.6838	-118.7219	2435	std	3	2.7	0.9958	0	8.65E+05	1.98E+04
Duffer Peak recessional										
PF-05	41.6809	-118.7167	2440	std	2	2.7	0.9851	0	4.56E+05	1.26E+04

Aluminum atoms and errors were disregarded for the purpose of showing this table. Accelerator mass spectrometry beryllium standard 07KNSTD was used for all samples.

Table B2. Cosmogenic ^{10}Be surface exposure age results using the Cronus-Earth online calculator developed by Balco et al. 2008.

Sample name	*Global 2016 Be-10 production rate, ERA atmosphere*					*Lifton et al 2015 Promontory Point Be-10 production rate, ERA atmosphere*				
	LSDn age (yr)	Int. uncert. (yr)	Ext. uncert. (yr)	LSDn age (ka)	Int. uncert. (ka)	PP-LSDn age (yr)	Int. uncert. (yr)	Ext. uncert. (yr)	PP-LSDn age (ka)	Int. uncert. (ka)
SANTA ROSA RANGE										
Granite Peak terminal										
SRSA-14	18676	785	1357	**18.7**	**0.8**	18144	763	1026	**18.1**	**0.8**
SRSA-15	17338	646	1213	**17.3**	**0.6**	16846	627	894	**16.9**	**0.6**
SRSA-16	17905	765	1308	**17.9**	**0.8**	17394	743	992	**17.4**	**0.7**
SRSA-17	17827	642	1236	**17.8**	**0.6**	17319	624	905	**17.3**	**0.6**
SRSA-18	19196	936	1474	**19.2**	**0.9**	18655	910	1152	**18.7**	**0.9**
			ave ± st dev	**18.2**	**0.7**			*ave ± st dev*	**17.7**	**0.7**
Granite Peak recessional										
SRSA-8	16232	655	1164	**16.2**	**0.7**	15750	636	871	**15.8**	**0.6**
SRSA-9	16468	643	1168	**16.5**	**0.6**	15997	624	869	**16**	**0.6**
SRSA-21	17200	589	1177	**17.2**	**0.6**	16703	572	852	**16.7**	**0.6**
SRSA-22	17450	777	1293	**17.5**	**0.8**	16960	755	991	**17**	**0.8**
SRSA-24	16451	659	1176	**16.5**	**0.7**	15978	640	880	**16**	**0.6**
SRSA-25	15628	501	1052	**15.6**	**0.5**	15183	486	753	**15.2**	**0.5**
			ave ± st dev	**16.6**	**0.7**			*ave ± st dev*	**16.1**	**0.6**
PINE FOREST RANGE										
Duffer Peak terminal										
PF-08	21701	574	1410	**21.7**	**0.6**	21120	559	976	**21.1**	**0.6**
PF-09	21576	565	1399	**21.6**	**0.6**	20994	550	967	**21**	**0.6**
PF-10	20482	532	1326	**20.5**	**0.5**	19909	517	914	**19.9**	**0.5**
PF-11	21826	617	1434	**21.8**	**0.6**	21244	601	1004	**21.2**	**0.6**
PF-12	33182	766	2117	**33.2**	**0.8**	32021	739	1423	**32**	**0.7**
			ave ± st dev	**21.4**	**0.6**			*ave ± st dev*	**20.8**	**0.6**
Duffer Peak recessional										
PF-05	18076	502	1183	**18.1**	**0.5**	17557	487	824	**17.6**	**0.5**
			ave ± st dev	**18.1**	**0.5**			*ave ± st dev*	**17.6**	**0.5**

LSDn is the Lifton-Sato-Dunai nuclide dependent scaling scheme used with the Promontory Point and global compilation production rate calibration datasets from Lifton et al. (2015) and Borchers et al. (2016).

APPENDIX C: MODELED ICE EXTENT OUTPUTS

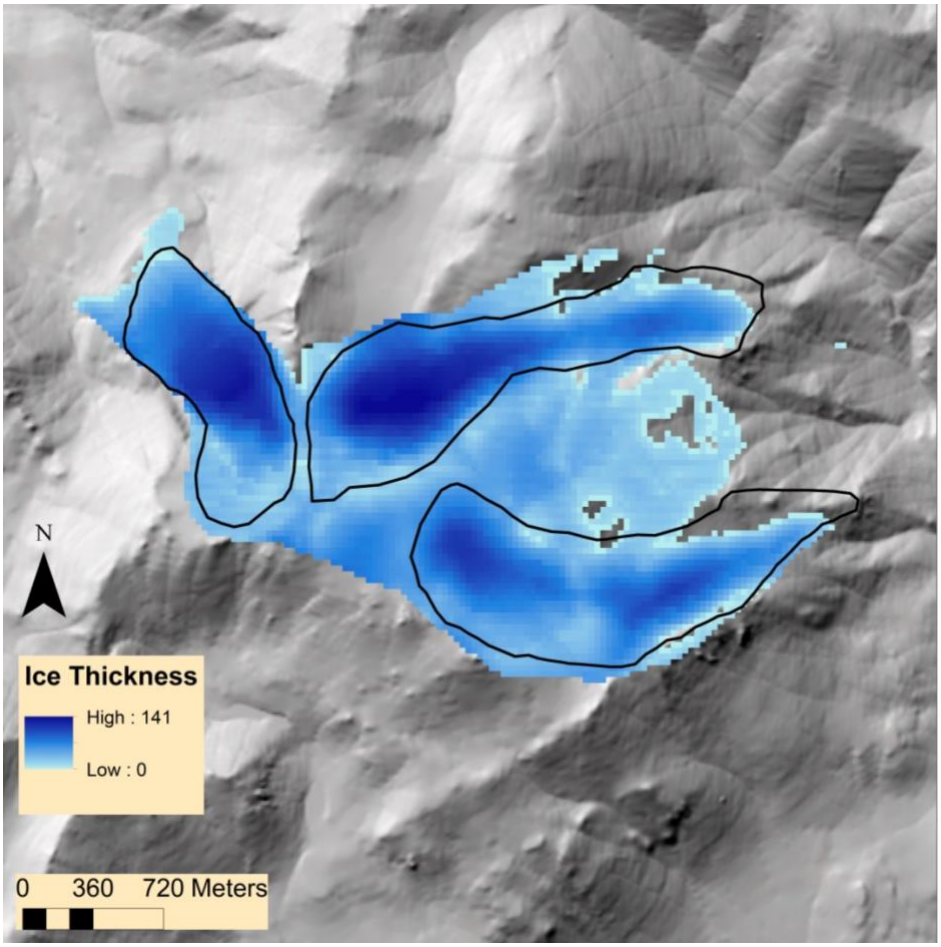

Figure C1. The reconstructed ice extents (black outline) and the modeled ice extents are shown for the terminal moraine of the Pine Forest Range, Nevada. The temperature-precipitation combination used for this modeled output was T-7.15°C, Px2.

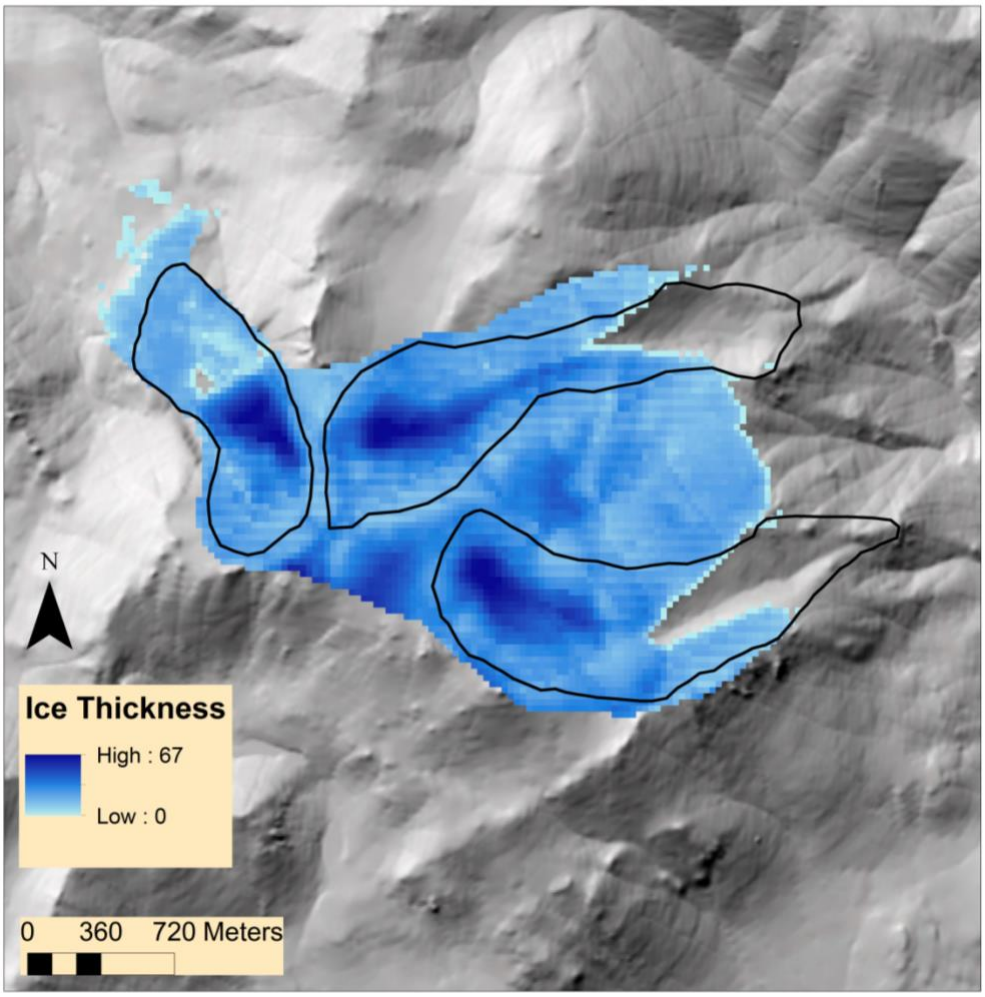

Figure C2. The reconstructed ice extents (black outline) and the modeled ice extents are shown for the terminal moraine of the Pine Forest Range, Nevada. The temperature-precipitation combination used for this modeled output was T-10.4°C, Px0.5.

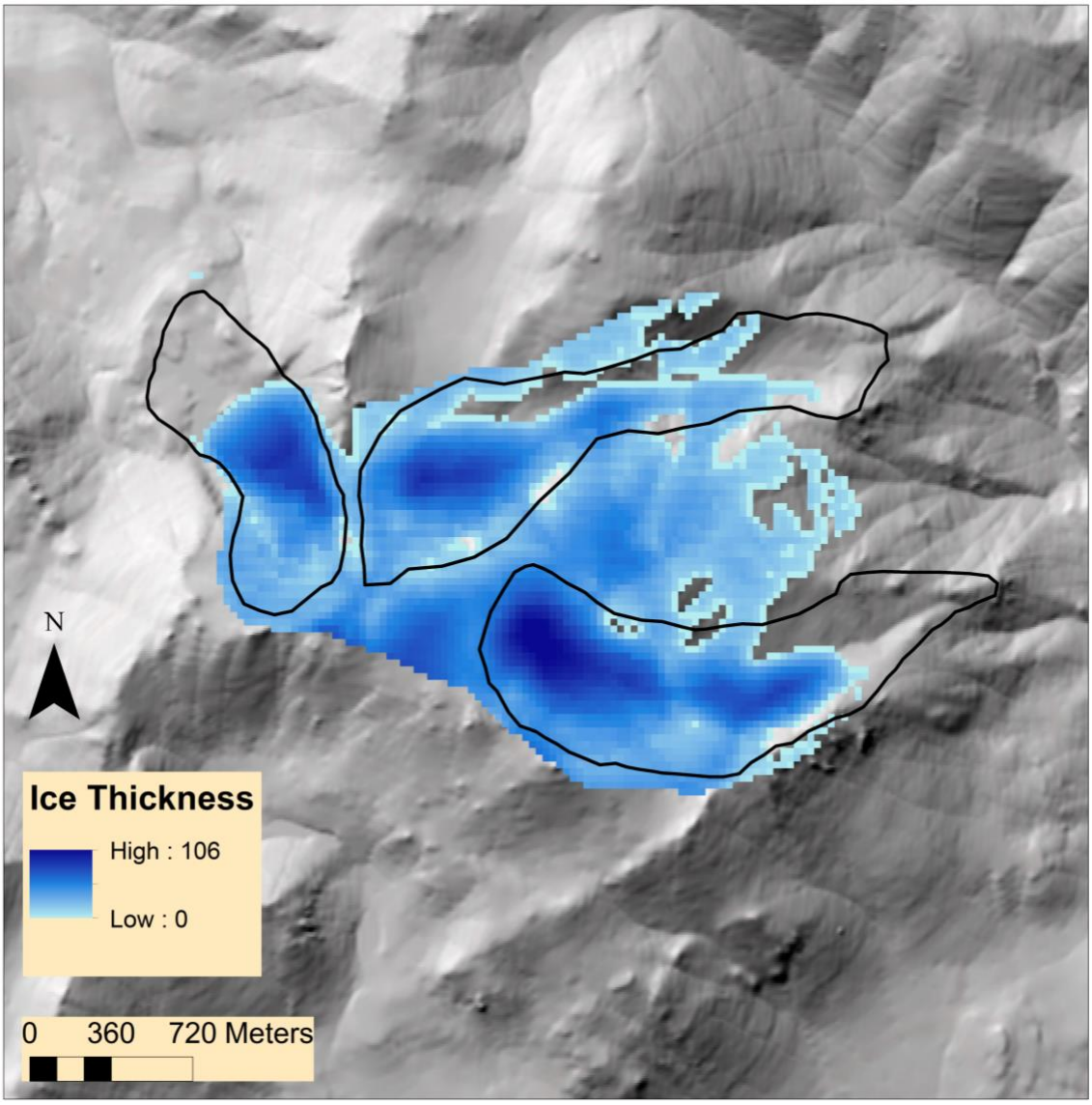

Figure C3. The reconstructed ice extents (black outline) and the modeled ice extents are shown for the recessional moraine of the Pine Forest Range, Nevada. The temperature-precipitation combination used for this modeled output was T-6.7°C, Px2.

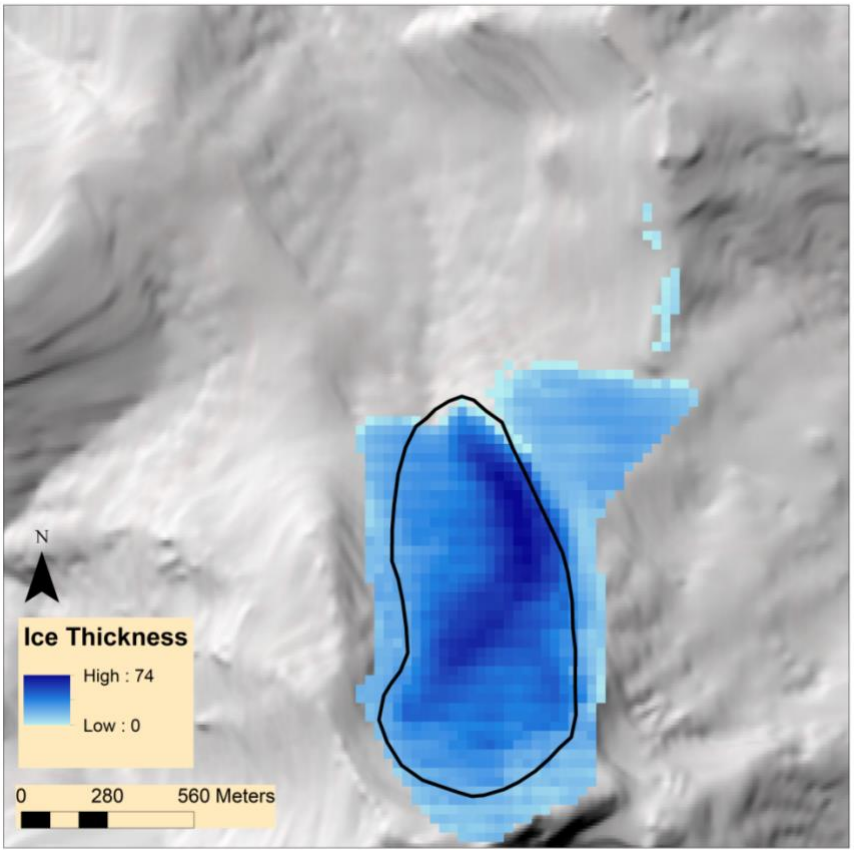

Figure C4. The reconstructed ice extent (black outline) and the modeled ice extent is shown for the terminal moraine of the Santa Rosa Range, Nevada. The temperature-precipitation combination used for this modeled output was T-8.05°C, Px0.5.

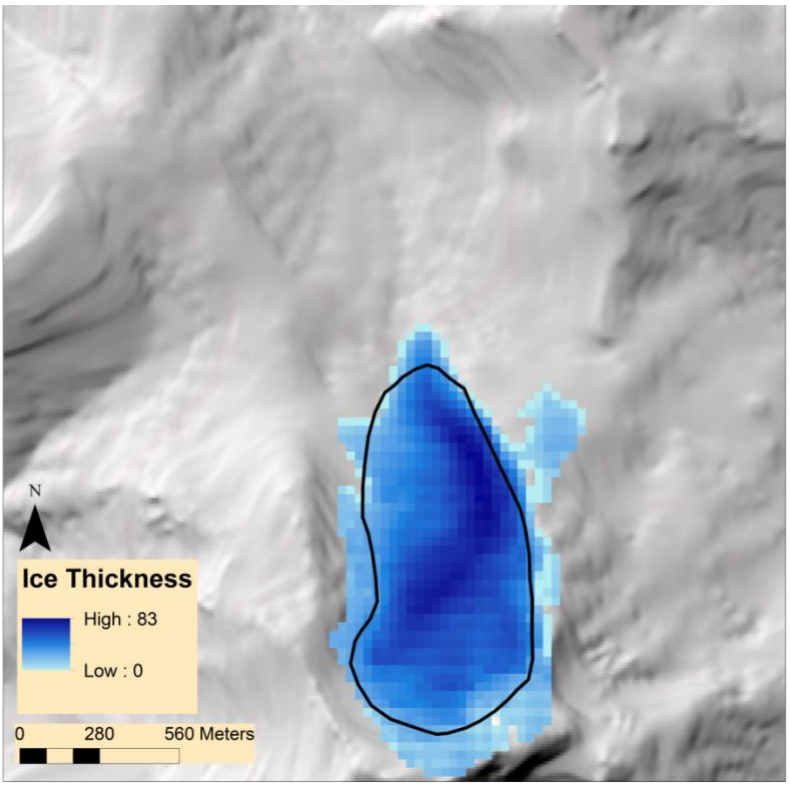

Figure C5. The reconstructed ice extent (black outline) and the modeled ice extent is shown for the terminal moraine of the Santa Rosa Range, Nevada. The temperature-precipitation combination used for this modeled output was T-4.35°C, Px2.

APPENDIX D: INPUT DATA FOR GLACIER AND LAKE MODELING

Table D1. Lake Franklin water balance model

Lake Franklin Highstand (in m)	Temperature Depression (°C)	CapaS Value of	Precipitation Factor
1850	0	2420	2.7468
1850	-2.5	2420	2.3058
1850	-5	2420	1.934
1850	-7.5	2420	1.6248
1850	-10	2420	1.2667
1850	-12.5	2420	1.1443
1850	0	140	2.1324
1850	-2.5	140	1.7174
1850	-5	140	1.4171
1850	-7.5	140	1.1849
1850	-10	140	1.0064
1850	-12.5	140	0.9227
1843	0	2420	2.7122
1843	-2.5	2420	2.2774
1843	-5	2420	1.9109
1843	-7.5	2420	1.6061
1843	-10	2420	1.2535
1843	-12.5	2420	1.1327
1843	0	140	2.0568
1843	-2.5	140	1.6549
1843	-5	140	1.3692
1843	-7.5	140	1.1471
1843	-10	140	0.9841
1843	-12.5	140	0.9037
1830	0	2420	2.5369
1830	-2.5	2420	2.1314
1830	-5	2420	1.7902
1830	-7.5	2420	1.5067
1830	-10	2420	1.1802
1830	-12.5	2420	1.0676
1830	0	140	1.7893
1830	-2.5	140	1.4409
1830	-5	140	1.2082
1830	-7.5	140	1.0203
1830	-10	140	0.9025
1830	-12.5	140	0.8314

Temperature and precipitation combinations required to form pluvial lake Franklin at varying highstands and *CapaS* values using the Condom et al. (2004) water balance model.

Table D2. Glacier modeling results

Sample Name	Temperature Depression (℃)	Precipitation Factor
Seitz Canyon (Terminal)	-13	0.5
	-11	0.8
	-10.8	1
	-9.5	1.5
	-9	1.75
	-8.5	2
Seitz Canyon (Recessional)	-10.5	1
	-9	1.5
	-8.5	1.85
	-8	2
Overland (Terminal)	-11	0.55
	-10	0.9
	-9.2	1
	-8	1.78
	-7	3.18
	-12	0.23
Overland (Recessional)	-11	0.25
	-10	0.55
	-9	0.9
	-8	1.6
	-7	2.4
Angel Lake (17ka)	-5	2.5
	-6	2
	-7	1.5
	-8.5	1
	-9.25	0.75
	-10	0.5
	-12	0.2
Pine Forest (Terminal)	-9.1	1
	-10.4	0.5
	-8	1.5
	-7.15	2
Pine Forest (recessional)	-8.7	1
	-10	0.5
	-7.5	1.5
	-6.7	2
Santa Rosa (17-18 ka)	-6.1	1
	-8.05	0.5
	-5.15	1.5
	-4.35	2

Temperature depression and precipitation solutions for the Seitz (Truong et al. 2014), Angel Lake (Bradley et al. 2015), Overland (Reimers et al. 2016), Pine Forest, and Santa Rosa glacier models.

Table D3. Solar Angles input data file for glacier modeling of the Pine Forest glaciers at 17ka.

"Month"	"E-S Correction"	"Daylength (hr)"	"Maximum Rad"	"Angles Int"	"AvgOPath"	"Blank"
1	1.017	9.277	158	1.325	4.893	0
2	1.033	10.39	226.9	1.485	4.094	0
3	1.041	11.8	324.4	1.686	3.475	0
4	1.037	13.21	418.4	1.887	3.172	0
5	1.024	14.41	482.9	2.059	3.09	0
6	1.005	15.04	504.3	2.148	3.096	0
7	0.9843	14.75	480.6	2.107	3.09	0
8	0.9684	13.72	420.1	1.961	3.12	0
9	0.9612	12.38	336.8	1.769	3.318	0
10	0.9643	10.97	247.4	1.567	3.795	0
11	0.9772	9.691	173.8	1.384	4.559	0
12	0.9964	8.974	139.5	1.282	5.169	0
126.1	141.5	159.7	180	200.3	218.5	233.9
115.4	132.8	154.4	180	205.6	227.2	244.6
100.7	119.9	145.6	180	214.4	240.1	259.3
85.78	105.6	133.7	180	226.3	254.4	274.2
73.74	93.51	121.1	180	238.9	266.5	286.3
67.95	87.59	114	180	246	272.4	292
70.59	90.29	117.4	180	242.6	269.7	289.4
80.52	100.4	128.6	180	231.4	259.6	279.5
94.53	114.1	141.1	180	218.9	245.9	265.5
109.5	127.7	151.1	180	208.9	232.3	250.5
122.3	138.4	157.9	180	202.1	221.6	237.7
128.8	143.6	160.9	180	199.1	216.4	231.2
6.248	16.97	24.29	26.92	24.29	16.97	6.248
7.729	21.5	31.41	35.12	31.41	21.5	7.729
9.374	27.04	40.96	46.65	40.96	27.04	9.374
10.43	31.37	49.77	58.36	49.77	31.37	10.43
10.74	33.54	55.51	67.54	55.51	33.54	10.74
10.7	34.1	57.63	71.82	57.63	34.1	10.7
10.73	33.89	56.72	69.88	56.72	33.89	10.73
10.63	32.48	52.46	62.41	52.46	32.48	10.63
9.898	29.04	44.79	51.54	44.79	29.04	9.898
8.454	23.85	35.32	39.75	35.32	23.85	8.454
6.801	18.63	26.84	29.83	26.84	18.63	6.801
5.848	15.8	22.5	24.89	22.5	15.8	5.848

This datafile was written by Mathcad.

Table D4. Solar Angles input data file for glacier modeling of the Pine Forest glaciers at 21ka

"Month"	"E-S Correction"	"Daylength (hr)"	"Maximum Rad"	"Angles Int"	"AvgOPath"	"Blank"
1	1.04	9.361	166.1	1.337	4.821	0
2	1.035	10.44	230.1	1.491	4.068	0
3	1.02	11.81	318.4	1.687	3.474	0
4	1.001	13.18	401.6	1.882	3.176	0
5	0.9816	14.34	459.1	2.049	3.091	0
6	0.9674	14.94	481.3	2.135	3.093	0
7	0.9622	14.66	465.8	2.095	3.089	0
8	0.9671	13.67	416.8	1.954	3.124	0
9	0.9809	12.37	343.1	1.768	3.32	0
10	1	11	258.4	1.572	3.782	0
11	1.02	9.76	185.3	1.394	4.508	0
12	1.034	9.07	149.7	1.296	5.079	0
125.3	140.9	159.3	180	200.7	219.1	234.7
115	132.4	154.1	180	205.9	227.6	245
100.7	119.8	145.5	180	214.5	240.2	259.3
86.13	106	134	180	226	254	273.9
74.43	94.22	122	180	238	265.8	285.6
68.82	88.48	115.1	180	244.9	271.5	291.2
71.38	91.1	118.3	180	241.7	268.9	288.6
81.01	100.9	129.1	180	230.9	259.1	279
94.64	114.2	141.1	180	218.9	245.8	265.4
109.2	127.5	150.9	180	209.1	232.5	250.8
121.6	137.9	157.5	180	202.5	222.1	238.4
127.9	143	160.5	180	199.5	217	232.1
6.36	17.3	24.79	27.5	24.79	17.3	6.36
7.787	21.68	31.71	35.48	31.71	21.68	7.787
9.38	27.06	41	46.69	41	27.06	9.38
10.42	31.29	49.58	58.09	49.58	31.29	10.42
10.74	33.45	55.22	67.02	55.22	33.45	10.74
10.71	34.04	57.34	71.18	57.34	34.04	10.71
10.74	33.81	56.43	69.3	56.43	33.81	10.74
10.62	32.39	52.22	62.03	52.22	32.39	10.62
9.89	29	44.72	51.45	44.72	29	9.89
8.488	23.96	35.51	39.98	35.51	23.96	8.488
6.893	18.9	27.27	30.33	27.27	18.9	6.893
5.974	16.17	23.06	25.52	23.06	16.17	5.974

The datafile was written by Mathcad.

Table D5. Solar Angles input data file for glacier modeling of the Santa Rosa glacier at 17-18ka.

"Month"	"E-S Correction"	"Daylength (hr)"	"Maximum Rad"	"Angles Int"	"AvgOPath "	"Blank"
1	1.027	9.299	160.7	1.328	4.873	0
2	1.038	10.41	228.9	1.487	4.086	0
3	1.04	11.8	324.4	1.686	3.474	0
4	1.031	13.2	415.4	1.886	3.172	0
5	1.014	14.39	477.2	2.056	3.09	0
6	0.9934	15.01	497.6	2.145	3.095	0
7	0.975	14.73	475.1	2.104	3.089	0
8	0.9634	13.71	417.4	1.959	3.12	0
9	0.9618	12.38	337	1.769	3.318	0
10	0.9705	10.98	249.5	1.569	3.79	0
11	0.9872	9.709	176.6	1.387	4.544	0
12	1.008	9	142.3	1.286	5.144	0
0	0	0	0	0	0	0
125.9	141.3	159.6	180	200.4	218.7	234.1
115.3	132.7	154.3	180	205.7	227.3	244.7
100.7	119.9	145.5	180	214.5	240.1	259.3
85.86	105.7	133.8	180	226.2	254.3	274.1
73.91	93.67	121.3	180	238.7	266.3	286.1
68.17	87.79	114.3	180	245.7	272.2	291.8
70.78	90.48	117.6	180	242.4	269.5	289.2
80.64	100.5	128.7	180	231.3	259.5	279.4
94.55	114.1	141.1	180	218.9	245.9	265.4
109.4	127.6	151	180	209	232.4	250.6
122.1	138.3	157.8	180	202.2	221.7	237.9
128.6	143.4	160.8	180	199.2	216.6	231.4
0	0	0	0	0	0	0
6.279	17.06	24.42	27.08	24.42	17.06	6.279
7.746	21.55	31.5	35.23	31.5	21.55	7.746
9.379	27.06	40.99	46.68	40.99	27.06	9.379
10.43	31.36	49.74	58.31	49.74	31.36	10.43
10.74	33.53	55.45	67.44	55.45	33.53	10.74
10.7	34.09	57.57	71.69	57.57	34.09	10.7
10.74	33.87	56.66	69.76	56.66	33.87	10.74
10.63	32.47	52.42	62.34	52.42	32.47	10.63
9.899	29.04	44.79	51.54	44.79	29.04	9.899
8.466	23.89	35.38	39.82	35.38	23.89	8.466
6.827	18.7	26.96	29.97	26.96	18.7	6.827
5.882	15.9	22.65	25.06	22.65	15.9	5.882

The datafile was written by Mathcad.

The required climate input file for the Energy mass balance (EMB) model that must be in the format 12 rows (one for each month, beginning at the start of the water year; October in Northern Hemisphere) with 11 columns:

1. Precipitation gradient y-intercept (m)
2. Precipitation gradient coefficient (m/m)
3. Precipitation gradient coefficient for square term (0 if linear regression)
4. Mean temperature (°C)
5. The standard deviation of daily mean temperatures for each month (°C)
6. Cloudiness (decimal % for the number of cloudy days per month)
7. Mean relative humidity (decimal %)
8. Mean wind speed (m/s)
9. Temperature lapse rate gradient y-intercept (°C)
10. Temperature lapse rate gradient coefficient (°C/m)
11. Temperature lapse rate gradient coefficient for squared term (0 if linear regression)

Table D6. Climate input data for the Pine Forest glacier modeling following the above requirements

-0.007	1.56E-05	0	8.24	5.12	0.16	0.42	2.53	18.98	-0.0057	0
-0.040	4.36E-05	0	2.03	4.70	0.29	0.62	2.01	10.51	-0.0048	0
-0.036	4.42E-05	0	-1.67	4.39	0.35	0.71	1.76	4.61	-0.0036	0
-0.024	3.69E-05	0	-0.88	4.05	0.33	0.71	1.62	5.25	-0.0041	0
-0.030	3.80E-05	0	-0.18	4.14	0.32	0.65	2.12	9.81	-0.0055	0
-0.044	4.95E-05	0	2.56	4.11	0.33	0.54	2.79	13.84	-0.0064	0
-0.028	3.44E-05	0	4.94	4.70	0.27	0.47	3.06	18.79	-0.0073	0
-0.015	2.71E-05	0	9.69	5.26	0.22	0.43	3.14	23.32	-0.0073	0
0.006	1.14E-05	0	13.85	6.32	0.15	0.34	3.26	28.11	-0.0073	0
0.006	2.48E-06	0	19.86	5.17	0.06	0.25	3.10	32.71	-0.0072	0
0.002	6.75E-06	0	19.11	4.61	0.06	0.24	2.92	31.18	-0.0065	0
-0.004	1.25E-05	0	15.16	4.57	0.10	0.29	2.78	25.55	-0.0059	0

Table D7. Climate input data for the Santa Rosa glacier modeling following the above requirements

-0.051	6.15E-05	0	4.02	6.04	0.20	0.37	3.02	21.89	-0.0073	0
-0.027	4.90E-05	0	-1.44	5.50	0.35	0.54	2.88	13.39	-0.0062	0
-0.078	7.98E-05	0	-4.34	5.22	0.40	0.62	2.59	7.54	-0.0050	0
-0.023	4.26E-05	0	-3.59	4.91	0.37	0.63	2.47	8.83	-0.0058	0
0.003	2.84E-05	0	-4.09	4.79	0.38	0.57	2.90	12.30	-0.0066	0
0.008	1.20E-05	0	-2.19	4.34	0.43	0.49	3.81	16.15	-0.0076	0
0.007	2.89E-06	0	0.05	4.83	0.41	0.45	3.77	20.93	-0.0085	0
0.017	-1.50E-06	0	4.76	5.01	0.30	0.41	3.57	25.16	-0.0085	0
0.008	9.55E-06	0	9.48	5.27	0.15	0.32	3.62	30.29	-0.0085	0
-0.004	2.16E-05	0	15.14	3.83	0.05	0.22	3.51	34.57	-0.0081	0
-0.041	6.01E-05	0	14.31	3.63	0.06	0.21	3.42	34.37	-0.0080	0
-0.049	6.45E-05	0	10.31	4.68	0.12	0.27	3.25	29.20	-0.0078	0